AD_____

Award Number: DAMD17-02-1-0307

TITLE: Electroacoustic Tissue Imaging

PRINCIPAL INVESTIGATOR: Gerald J. Diebold, Ph.D.

CONTRACTING ORGANIZATION: Brown University
                            Providence, RI   02912

REPORT DATE: April 2005

TYPE OF REPORT: Annual

PREPARED FOR: U.S. Army Medical Research and Materiel Command
               Fort Detrick, Maryland   21702-5012

DISTRIBUTION STATEMENT: Approved for Public Release;
                        Distribution Unlimited

The views, opinions and/or findings contained in this report are
those of the author(s) and should not be construed as an official
Department of the Army position, policy or decision unless so
designated by other documentation.

20050712 014

REPORT DOCUMENTATION PAGE

Public reporting burden for this collection of information is estimated to average 1 hour per response, including the time for reviewing instructions, searching existing data sources, gathering and maintaining the data needed, and completing and reviewing this collection of information. Send comments regarding this burden estimate or any other aspect of this collection of information, including suggestions for reducing this burden to Washington Headquarters Services, Directorate for Information Operations and Reports, 1215 Jefferson Davis Highway, Suite 1204, Arlington, VA 22202-4302, and to the Office of Management and Budget, Paperwork Reduction Project (0704-0188), Washington, DC 20503

1. AGENCY USE ONLY	2. REPORT DATE	3. REPORT TYPE AND DATES COVERED
	April 2005	Annual(1 Apr 2004 - 31 Mar 2005)

4. TITLE AND SUBTITLE
Electroacoustic Tissue Imaging

5. FUNDING NUMBERS
DAMD17-02-1-0307

6. AUTHOR(S)

Gerald J. Diebold, Ph.D.

7. PERFORMING ORGANIZATION NAME(S) AND ADDRESS(ES)
Brown University
Providence, RI 02912

E-Mail: Gerald_Diebold@Brown.edu

8. PERFORMING ORGANIZATION REPORT NUMBER

9. SPONSORING / MONITORING AGENCY NAME(S) AND ADDRESS(ES)

U.S. Army Medical Research and Materiel Command
Fort Detrick, Maryland 21702-5012

10. SPONSORING / MONITORING AGENCY REPORT NUMBER

11. SUPPLEMENTARY NOTES

12a. DISTRIBUTION / AVAILABILITY STATEMENT
Approved for Public Release; Distribution Unlimited

12b. DISTRIBUTION CODE

13. ABSTRACT (Maximum 200 Words)

The goal of this research has been to develop new methods of imaging tumors. The primary effort has been in developing an imaging method based on the ultrasonic vibration potential. We have formulated a complete theory of image formation for an arbitrary shape object irradiated by a plane wave. Experiments have been carried out that verify the theory and demonstrate straightforward examples of the use of the method. Work has focused on construction and optimization of an apparatus for scanning a transducer and recording images. Additionally, we have investigated the use of phase contrast x-ray imaging for tumor detection using ultrasonic radiation pressure to modify x-ray phase contrast images. Experiments have been carried out with phantoms to demonstrate the method.

14. SUBJECT TERMS
Vibration potential, ultrasound, phase contrast, imaging

15. NUMBER OF PAGES
33

16. PRICE CODE

17. SECURITY CLASSIFICATION OF REPORT	18. SECURITY CLASSIFICATION OF THIS PAGE	19. SECURITY CLASSIFICATION OF ABSTRACT	20. LIMITATION OF ABSTRACT
Unclassified	Unclassified	Unclassified	Unlimited

Table of Contents

INTRODUCTION

The ultrasonic vibration potential, originally predicted by Debye[1] in 1933, refers to voltage generated when a colloidal or ionic solution irradiated with ultrasound. In a colloid, the voltage production is the result of differential motion between the particles in suspension and the surrounding fluid. Colloids are suspensions of charged particles in solution. Some examples include milk, muddy water, and India ink. Normally the counter charge around each particle is spherical; however when a sound wave propagates through the suspension, there is a differential motion of the particles and the fluid owing to their different inertias. Typically, the particles are dense, and tend to remain stationary in space. The result of the differential motion is that the fluid oscillates back and forth over the surface of the particles. Since the counter charge moves with the fluid, an electric dipole is created at the site of each particle owing to the distortion of the normally spherical charge distribution. Over a macroscopic length, the polarization from addition of the dipoles results in a voltage that can be measured with a pair of electrodes in solution.

We have found that whole blood generates a signal that is substantial compared with animal tissue. The potential benefit of the method relative to conventional x-ray and ultrasonic imaging is the contrast that should be obtainable in a vibration potential image would come from the presence of blood, which is a marker for many invasive tumors. The resolution of the method is governed ultimately by the wavelength of the ultrasound. In the experiments carried out with one-dimensional objects, the resolution using a frequency domain version of the instrument, resolution much higher than that dictated by the radiation wavelength is possible.

We have also investigated phase contrast x-ray imaging for tumor detection. The principle on which this kind of imaging relies is on a recording of the phase changes that x-rays experience on traversing a body. In principle, phase contrast measurement is on the order of 1000 times as sensitive as absorption contrast for most of the useful x-ray region of the spectrum. The idea of the method is old, but its application to the x-ray region of the spectrum in a convenient geometry was first reported by Wilkins and coworkers[9]. To observe phase contrast in an image using the "in-line" geometry introduced by Wilkins, the x-ray source must have high spatial coherence, but not necessarily high temporal coherence, that is, there is no severe consequence to using polychromatic x-rays. X-ray sources that have been developed for phase contrast imaging include the microfocus x-ray tube and the synchrotron, the former generating an approximation to a spherical wave, and the latter a plane wave.

In the in-line geometry, objects with differing densities induce different phase lags in the x-rays as they traverse a body that are manifested by deflection of the x-rays and the formation of interference fringes in the image. The peculiar feature of phase contrast imaging is the highlighting of objects with different densities with a sharp outline in the image. Our method uses ultrasonic radiation pressure to produce displacements in an object. The method we use for generating an image is to take a single x-ray image using a CCD camera and to transfer the image to a computer. Next a second x-ray image is made but in the presence of the ultrasound. The two images are subtracted pixel by pixel in the computer to form the final image. The subtraction results in a heightening of the phase contrast features of the image and a removal of

4

the absorption features. The utility of the method for tumor imaging is that the tumor, owing to its mechanical properties moves as a unit in response to the ultrasound. Often physicians use the same mechanical property of tumors in what is referred to as "palpation" to locate the presence of tumors in soft tissue through use of finger pressure. The perception of a tissue mass that moves as a unit indicates the possible presence of a tumor. Since tumors have different elastic properties from healthy tissue, their sound speed differs from that of the surrounding tissue so that a differential radiation force is experienced by the tumor. The objective of the approach under investigation here is to combine the high spatial resolution of x-ray mammography with the specificity of palpation to produce an image that highlights objects that move as a unit.

BODY

The qualitative explanation given above for generation of the ultrasonic vibration potential by a colloid has been investigated by a number of authors since its prediction by Debye. Reviews have been published by Povey[3], Zana and Yeager[4], Babchin, Chow and Sawatzky,[5] and O'Brien, Cannon, and Rowlands[6-9]. The theory of the vibration potential for dilute suspensions of O'Brien and coworkers[6-9] is more rigorous than any other formulation, and is widely accepted by workers in the field. According to O'Brien's theory, the electric field across a region of the colloid generated by a pressure gradient ∇p is given by,

$$\mathbf{E} = \frac{f \, \Delta\rho_m \, \mu_E}{\rho_m \, \sigma^*} \nabla p, \tag{1}$$

where $\Delta\rho_m$ is the difference between the densities of particle and the fluid, f is the volume fraction of the particles, μ_E is dynamic mobility of the particle, σ^* is the conductivity, and ρ_m is the fluid density. Vibration potential imaging is based on generation of a voltage across a pair of electrodes by an ultrasonic wave that traverses the body. The important part of the research conducted here is to determine the presence of a colloidal or ionic fluid within a body and to determine its distance from the electrodes and its geometry. This requires a complete theory of image formation, the starting point for which is Eq. 1.

The work with phase contrast imaging has focused on setting up a laboratory provided with a microfocus x-ray tube, a liquid nitrogen cooled CCD camera, fiber optic scintillator plate, optics, and sample mounts. The apparatus is interfaced with a computer so that the x-ray tube can be turned on and off remotely, and the CCD image transferred to the computer for storage. The method of producing an image in these experiments is to take a single phase contrast image of the body, and to store the image in a computer. Second, ultrasound is applied to the body that moves objects having densities or sound speeds different from that of the body. The resulting radiation force causes a movement of the object so that a second image records a modified image. The two x-ray images are then subtracted, resulting in an image that has most of the absorption component of the image removed, but with a highlighted phase contrast component left in the image.

KEY RESEARCH ACCOMPLISHMENTS

The theory of production of a vibration potential image has been formulated (see "Imaging with the Ultrasonic Vibration Potential": A Theory for Current Generation",

Ultrasound in Med & Biol., Appendix I) for an experimental arrangement where parallel electrodes are placed around the body, and the sound beam propagates perpendicularly to the plates. The object is considered to lie within a limited region of the body, and the dielectric constant and the conductivity of the body are considered to be uniform. The main conclusion of the theory thus far formulated is that the current in the electrodes is given by

$$I = \frac{i\omega}{h} \int_V \alpha(\mathbf{x}, \omega) \frac{\partial}{\partial z} p(\mathbf{x}) \, dx \, dy \, dz.$$

(2)

which can be expressed as

$$I = -\frac{i\omega}{h} \int_V [\nabla\alpha(\mathbf{x}, \omega)]_z \, p(\mathbf{x}) \, dx \, dy \, dz.$$

(3)

where α is the distribution of the colloid in space, ω is the frequency of the ultrasound, h is the distance between the electrodes, and p is the pressure.

Equations 2 and 3 form the basis for vibration potential imaging. For the first experiments we have looked at straightforward rastering of the transducer to produce amplitude images. The apparatus is shown in Fig 1 of Appendix II ("Imaging based on the Ultrasonic Vibration Potential" *Appl. Phys. Lett*) The paper describes two methods of imaging, one based on time of appearance of the vibration potential, and a second method based on changing small changes in frequency. Our approach thus far in this research has been to take colloidal objects that have specific geometries and to predict the frequency dependence of the in phase and quadrature components of the current to confirm the theory and to explore fundamental properties of the imaging. Figs 1 and 2 show some recent images taken with silica phantoms in agarose.
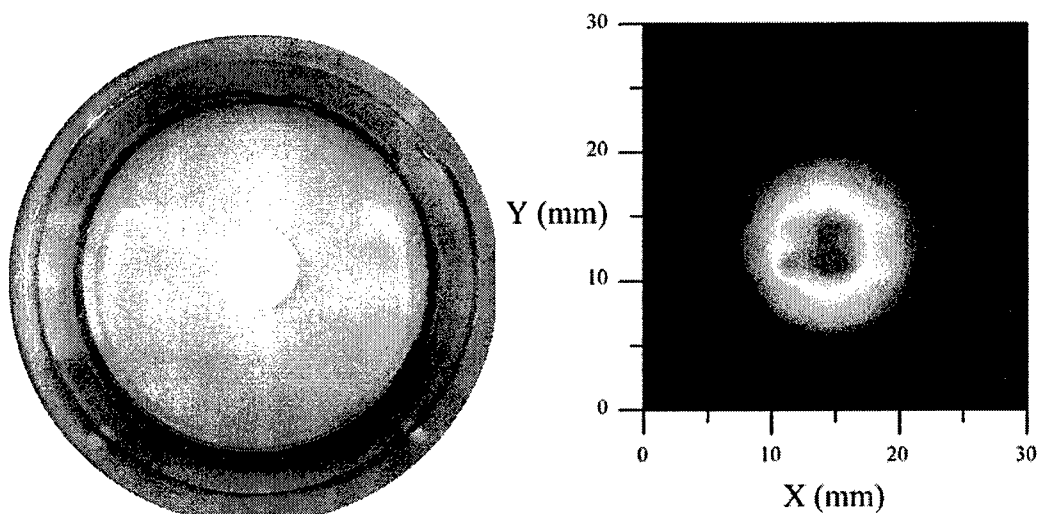

Fig. 1 (Left) Photograph of a top view of a two silica colloid discs, one beneath another. A side view of the phantom is shown in Fig 2. The image is obtained by scanning the focused transducer over a rectangle 30 mm by 30 mm. in 0.5 mm steps. The signal, after amplification in a low noise preamplifier, is sent to a lock-in amplifier. (Right) Vibration potential image of the phantom.
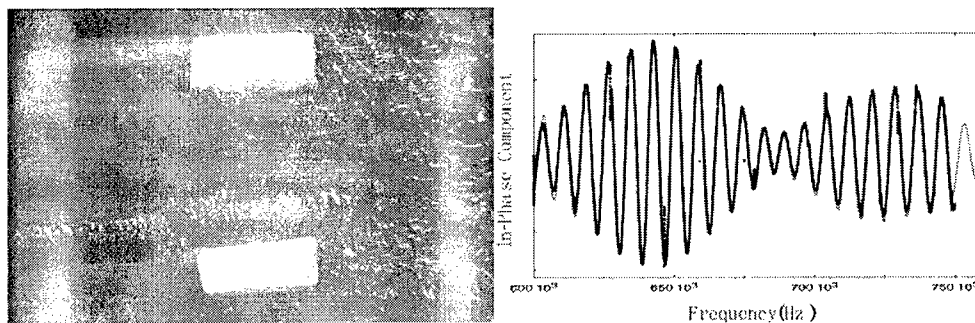
6

Fig: 2 (Left) Side view of the two silica colloid disk phantom. The 2D scanning in Fig. 1 can discern the top disk disc, but with the bottom one missing. Determination of the presence of the second disk is carried out by fixing the transducer at the center position and sweeping the frequency. By fitting the in-phase component of the signal, both the length and vertical position of each disk can be determined.

We have proven the feasibility of our method of subtractive imaging based on acoustic radiation pressure to modify phase contrast images. See Appendices III and IV. To date, our work has used a microfocus x-ray tube and a CCD camera with a phosphor screen to make x-ray images with phase contrast. It is well-known that the method requires spatial coherence in the x-ray source, as is produced by a synchrotron or a point radiation source. We are developing two approaches for providing point sources of radiation. We use a commercial microfocus x-ray tube for taking x-ray images at present, and have been developing a second source based on focusing a fs laser to generate x-rays.
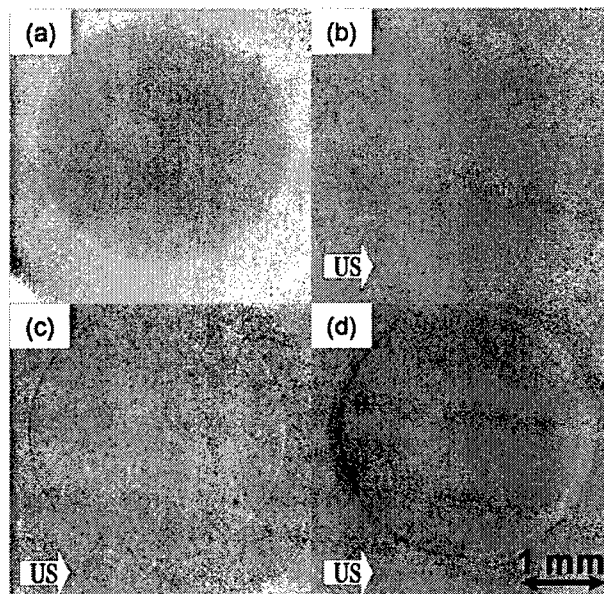
Figure 3: (a) Conventional phase contrast image of a 3.05 mm diameter Teflon sphere suspended by a glass fiber in water showing both absorption and phase contrast. (b)-(d), subtracted x-ray-acoustic phase contrast images taken with 10 kPa, 0.6 MPa, and 1.1 MPa average acoustic power applied to the transducer.

Results of using the method on a Teflon sphere in water are shown in Fig. The figures where the radiation force is 0.6 MPa and 1.1 MPa show the movement of the sphere by the radiation forces, and the virtual elimination of the absorptive component of the x-ray image.

KEY RESEARCH ACCOMPLISHMENTS

A rigorous theory of the formation of the vibration potential has been formulated. The theory has been applied to forming images of several objects. The results of this theory can be applied to model simple objects such as a spherical body, a cylindrical body, and a layer, or, in general, to any arbitrary object within a body. The method has been applied to form images of colloidal objects through use of the time of appearance of the vibration potential signal as well as a simple rastering over the surface of an object to give an "amplitude map" of the colloid in space. The results are summarized in Appendices I and II.

Acoustically modulated x-ray phase contrast images have been taken of Teflon spheres in agarose demonstrating the method, (as shown in Appendices III and IV) and giving a general estimate of the acoustic radiation pressure required to produce tissue movement of sufficient amplitude to be recorded within the resolution of the x-ray tube and CCD camera used here. Images of density modified agarose (agarose containing colloidal carbon) in chicken flesh have been recorded. See Appendices III and IV for details of the experiments.

REPORTABLE OUTCOMES

The following have been published or are under review:

"Vibration Potential Imaging: Theory and Preliminary Results", with A. C. Beveridge, S. Wang, and V. Gusev, Proc SPIE 2004; 5320: 95-100

"Vibration Potential Imaging" with V. Gusev, A. C. Beveridge, and S. Wang, Proc. NIST Conf. on Thermophysical Properties, Boulder, 2004

"Imaging based on the Ultrasonic Vibration Potential" with A. C. Beveridge and S. Wang, (*Appl. Phys. Lett.* **85**, 5466 (2004)

"Acoustic Radiation Pressure: a "Phase Contrast" Agent for X-ray Phase Contrast Imaging, with C. Bailat, T. Hamilton, C. Rose-Petruck *Appl. Phys. Lett* **85** 4517 (2004)

"Imaging with the Ultrasonic Vibration Potential: A Theory for Current Generation" with V. E. Gusev *Ultrasound in Med. and Biol.* 31, 273 (2005)

"The Theory of Ultrasonic Vibration Potential Imaging" A. C. Beveridge, S. Wang, and V. E. Gusev, *Journal de Physique IV*, accepted for publication)

"Acoustically Modulated X-Ray Phase Contrast Imaging" with T. Hamilton, and C. Bailat, C. Rose-Petruck, Phys. Med. Bio. **49**, 4985 (2004)

"Acoustically Modulated X-Ray Phase Contrast and Vibration Potential Imaging" with a. C. Beverideg, C. J. Bailat, T. J. Hamilton, S. Wang, C. Rose-Petruck, and V. E. Gusev (Proc. SPIE 2005, in press) selected as the best conference paper

CONCLUSIONS

An operating instrument for producing images using the ultrasonic vibration potential has been constructed. The theory of vibration potential imaging has been given for an arbitrary object. The method has been applied to form images. Phase contrast images using a microfocus tube with acoustic modulation of objects within a body have been made. Both imaging methods show promise for tumor detection.

REFERENCES

1. P. Debye, "A Method for the Determination of the Mass of Electrolytic Ions", J. Chem. Phys. 1, 13 (1933)
2. S. W. Wilkins, T. E. Gureyev, D. Gao, A. Pogany, and A. W. Stevenson, Nature 28, 384 (1996)
3. M. J. Povey, *Ultrasonic Techniques for Fluids Characterization* (Academic Press, San Diego, 1997) See Ch. 5.1.5.7, p 150
4. R. Zana and E. Yeager in "Modern Aspects of Electrochemistry" Vol. 14 (Plenum, New York, 1982), J. Bockris, B. Conway and R. White, eds.
5. A. J. Babchin, R. S. Chow and R. P. Sawatzky, "Electrokinetic Measurements by Electroacoustical Methods", Adv. in Colloid and Interface Sci. 111, 30, (1989)
6. R. W. O'Brien, D. W. Cannon, and W. N. Rowlands, J. Colloid and Interface Sci.173, 406 (1995);
7. R. W. O'Brien, Applied Mathematics Preprint, AM86/25 Univ. South Wales, 1985;
8. R. W. O'Brien, J. Fluid Mech.190, 71 (1988); R. W. O'Brien, J. Fluid Mech.212, 81 (1990);
9. R. W. O'Brien, P. Garside, and R. J. Hunter, Langmuir 10, 931 (1994)

APPENDIX

Four published papers are attached as appendices

Imaging based on the ultrasonic vibration potential

Andrew C. Beveridge, Shougang Wang, and Gerald J. Diebold[a)]
Department of Chemistry, Brown University, Providence, Rhode Island 02912

An ultrasonic wave traversing a colloidal suspension causes distortion of the charge distributions at the sites of individual colloidal particles producing a voltage known as the ultrasonic vibration potential. We show how imaging of colloidal regions within a body can be carried out using a beam of ultrasound to produce a radio frequency vibration potential. A theory for image formation shows that Fourier transformation of vibration potential signals processed by a mixer and low pass filter gives the spatial distribution of colloid. The salient feature of the method, insofar as medical imaging is concerned, is its contrast mechanism. © *2004 American Institute of Physics.*
[DOI: 10.1063/1.1827350]

Colloids are suspensions of charged particles in a liquid with a counter-charge distributed in the fluid around each particle. The counter-charge, which is normally a spherical distribution around the particles, gives the solution overall charge neutrality and, together with the charge on the particle surface, stabilizes the suspension against particle agglomeration. When sound propagates through a suspension where the particles have either a higher or lower density than that of the surrounding fluid, the amplitude and phase of the particle motion, owing to the difference in inertia between the particle and the volume of fluid it displaces, differs from that of the fluid so that fluid flows back and forth relative to the particle on alternating phases of the acoustic cycle. Since the counter-charge is carried by the fluid, the oscillatory motion of the fluid relative to the particle distorts the normally spherical counter-charge distribution creating an oscillating dipole at the site of each particle, which, when added over a half wavelength of the sound wave, results in a macroscopic voltage that can be recorded by a pair of electrodes placed in the solution. Similar considerations of particle inertia show that vibration potentials are generated in ionic solutions as well. The theory of the colloidal vibration potential[1–3] gives the electric field $\mathbf{E}$ generated by an acoustic pressure p as $\mathbf{E}=-(\varphi\Delta\rho\mu_E/\rho K^*)\,\nabla p$, where φ is the volume fraction of particles, $\Delta\rho$ is the density difference between the particles and the solvent, μ_E is the electrophoretic mobility of the particles, ρ is the solution density, and K^* is the conductivity of the suspension.[4] According to linear acoustics of an inviscid medium, the gradient of the pressure is related to the fluid acceleration $\ddot{\mathbf{u}}(\mathbf{r},t)$ through $\ddot{\mathbf{u}}=-\nabla p/\rho$, which, for a plane wave propagating along the z axis, can be written in terms of the displacement $\mathbf{u}(z,t)$ at a time t as $\ddot{\mathbf{u}}(z,t)=-\omega^2\mathbf{u}(z,t)$, where ω is the radial frequency of the wave. Since the potential across the region of integration $\Delta\Psi$ is given by $\Delta\Psi(t)=\int\mathbf{E}\cdot d\mathbf{z}$, it follows for a one-dimensional geometry[5,6] that

$$\Delta\Psi(t) = \Gamma \int \hat{u}(\hat{z},t)c(\hat{z})d\hat{z}, \qquad (1)$$

where the quantities in the integral marked with a hacek are dimensionless, i.e., $\hat{z}=z/L$ and $\hat{u}=u/u_0$, u_0 is the magnitude of the acoustic displacement in the plane wave, L is the

length of the colloidal region, and Γ is a proportionality constant given by $\Gamma=-\omega^2\varphi\Delta\mu_E u_0 L/\rho K^*$, with the integration extending over the spatial extent of the sound wave.

The apparatus used for vibration potential imaging, as shown in Fig. 1, consisted of a cell containing the object of interest, equipped with acoustic delay lines on the top and bottom of the cell, with two electrodes at opposite ends of the cell, mounted directly on the faces of the delay lines. One electrode was attached to an aluminum housing surrounding the cell, which forms a ground, and the other electrode was connected to a feedthrough and cable leading to a rf amplifier (Analog Devices, Inc. Model AD 8021) with a voltage amplification of 100. Ultrasound was generated by a
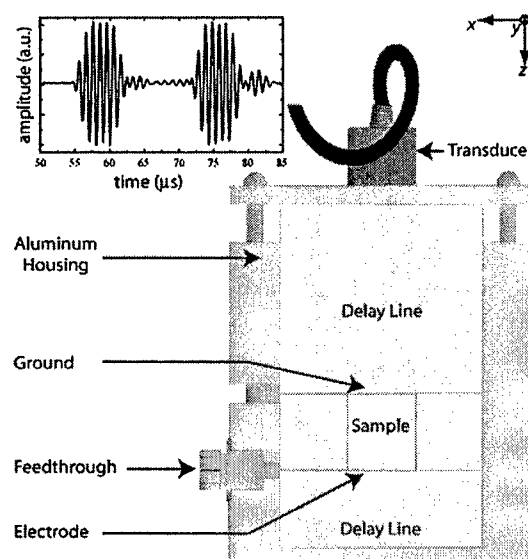

FIG. 1. Diagram of the apparatus. Ultrasound from the transducer enters and exits the colloidal region of the cell through a variable length (approximately 50 mm long) acoustic delay lines. An aluminum housing, which serves as the electrical ground, supports the cell and the delay lines. The delay lines were either acrylic blocks with copper tape electrodes mounted on the faces of the delay lines or water columns with 90 μm wires used as electrodes and plastic membranes used to separate the colloid from the water. For experiments where an image is generated, the transducer is scanned in the XY plane and the vibration potential signal after processing is stored in a computer as a function of position. Inset: Oscilloscope trace of vibration potential (in arbitrary units) vs time generated by approximately six pulses of 1 MHz ultrasound traversing a water delay line into a 2.538-cm-thick layer of colloidal silica.

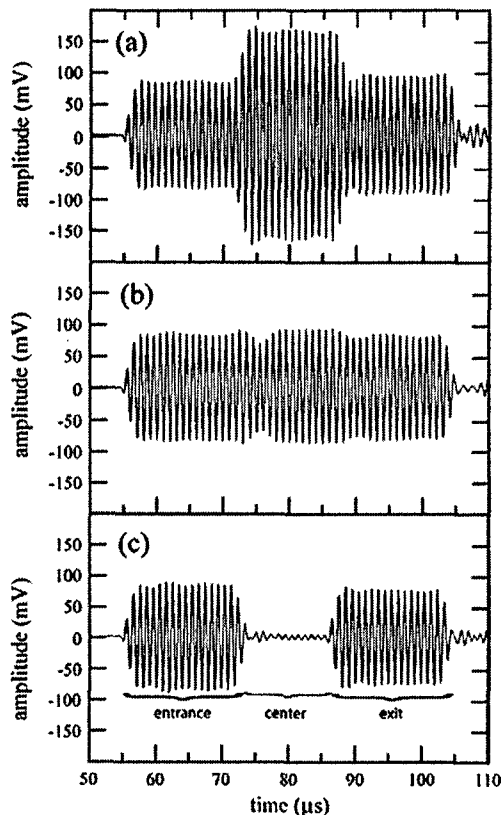[a)]Electronic mail: gerald_diebold@brown.edu

FIG. 2. Oscilloscope traces of the vibration potential generated by 32 pulses of (a) 1.0165 MHz, (b) 1.0069 MHz, and (c) 0.9865 MHz ultrasound traversing a saline solution delay line into 2.5-cm-thick layer of colloidal silica. Signals were averaged over 64 repetitions of the pulse burst. The oscilloscope voltage is referred to the electrodes after amplification. The initial (55–75 μs) and final (85–105 μs) parts of the wave forms correspond to entrance of the ultrasound into the colloidal layer and exit from the layer, respectively. The central portions of the wave forms show the effects of integration of the wave over the entire length of the colloidal layer. For the 0.9865 MHz trace, the colloidal layer thickness is an integral number of sound wavelengths giving complete cancellation of the voltage in the center of the wave form.

2.54-cm-diameter $LiNbO_3$ transducer driven by a programmable pulse generator, or by a function generator that drove a power amplifier.

An experiment was carried out where a short burst of ultrasound consisting of six cycles of a 1 MHz sine wave, generated at a repetition rate of 60 Hz, was applied to the cell which contained a 2.538-cm-thick colloidal layer. The spatial extent of the pulse burst was smaller than the length of the colloid layer in the cell. The signal from a colloidal silica sample[7] recorded by the oscilloscope is shown in the inset of Fig. 1. As the ultrasound burst either enters or leaves the colloid, an alternating vibration potential is produced. However, when the entire six cycles of the burst of ultrasound are totally confined within the colloidal region, the positive and negative contributions to the potential, in agreement with Eq. (1), integrate to zero giving a null voltage.

For bursts of ultrasound whose extent in space is larger than the thickness of the colloidal layer, the voltages from individual half-cycles of the sound wave, according to Eq. (1), can be nonzero or add to zero depending on thickness of the layer and the wavelength of sound. Figure 2 shows vibration potential signals at three different frequencies produced by a 32 cycle burst of ultrasound whose spatial extent

is large compared with the 2.538 cm layer thickness, showing the effect of voltage integration over the length of the cell. Evaluation of Eq. (1) for a wave that fills the colloidal region shows that the zeroes in the signal occur when $n\lambda = L$, where n is an integer, λ is the wavelength of the sound, and L is the length of the layer. It follows for two frequencies f_2 and f_1, which have zeroes for integer values of the wavelength n_2 and n_1, that $(n_2-n_1)c=L(f_2-f_1)$ where c is the sound speed which permits determination of the layer thickness. Data taken over a more extensive range than shown in Fig. 2, from 0.8984 to 1.0765 MHz, gave the length of colloid as 2.553 ± 0.025 cm.

There are three kinds of imaging that follow from Eq. (1) for determining the Z dependence (as defined in Fig. 1) of colloidal distributions in space for a focused transducer scanned in the XY plane. The first method uses the amplitude of the vibration potential recorded with a lock-in amplifier as the transducer is rastered in the XY plane to form an image. The second method, analogous to conventional pulse-echo imaging, is based on recording the delay time between the appearance of the vibration potential signal and the time of launching of the acoustic burst. The delay time, together with the sound speed, gives the distance between the colloidal object and the transducer. For the third method, consider an arbitrary distribution of colloid in space $c(z)$ traversed by a plane wave propagating in the Z direction. It is straightforward to show that accumulation of in-phase and quadrature voltages from a mixer and low pass filter, recorded over a range of k, or, equivalently, over a range of frequencies, gives the distribution of colloid in space, $c(z)$, through Fourier transformation as

$$c(z) = \frac{4}{\Gamma}\left[\int L_I(k)\cos(kz)dk + \int L_Q(k)\sin(kz)dk\right], \quad (2)$$

where $L_I(k)$ and $L_Q(k)$ are the in-phase and quadrature components of the signal following low pass filtering. Equation (2) shows that the vibration potential can be inverted to determine any arbitrary colloid distribution in space $c(z)$. It is noteworthy that a layer of uniform thickness extending along the z axis a distance L from the origin gives $L_I(k) = (\Gamma/2k)\sin(kL)$ and $L_Q(k)=(\Gamma/2k)[1-\cos(kL)]$, the first of which can be written in terms of the familiar sinc function as $L_I(k)=(\Gamma L/2)\text{sinc}(kL)$. The amplitudes of the central portions of the traces in Fig. 2 give three points on the sinc curve $L_I(k)$.

Experiments were carried out with objects to give a demonstration of vibration potential imaging. An agarose block containing colloidal discs was placed at the bottom of the cell with the agarose making contact with the electrode leading to the preamplifier. The apparatus shown in Fig. 1 was modified so that a saline solution in a cylindrical enclosure replaced the acrylic delay line at the top of the cell. The salt solution, which formed one of the electrodes for the cell, made contact with the metal housing of the cell providing both a ground for the rf signal and a delay line for a beam of ultrasound[8] from a 5.1-cm-diam, 15.2 cm focal length $LiNbO_3$ transducer (Valpey Fisher Model E1129). The ultrasound beam was approximately 3 mm in diameter beam over the length of the sample. The transducer was driven by a pulse generator that produced 900 kHz voltage bursts 28 μs long with a repetition rate of 50 Hz, amplified by a gated power amplifier. The position of the transducer relative to the
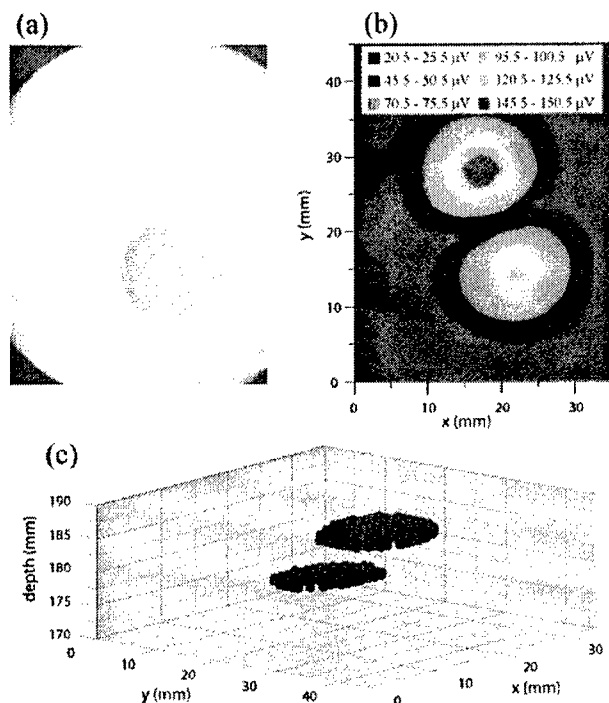
FIG. 3. (Color) (a) Photograph, (b) two-dimensional amplitude, and (c) three-dimensional surface vibration potential images of thin layer colloidal phantoms cast in agarose. In (c), plotted with the ultrasound beam propagating upwards, the depth was determined from the delay time of the vibration potential signal relative to the launching of the acoustic burst; only the upper surfaces of the colloidal objects are recorded. The XY scan data were recorded at intervals of 1 mm with an integration time at each pixel of 1 s. The driving voltage on the focused LiNbO$_3$ transducer was 250 V peak-to-peak.

phantoms in the cell was scanned by precision translation stages controlled by a computer. Signals from the preamplifier were fed to both a digitizer and a lock-in amplifier as transducer was rastered in the X and Y directions across the sample.

Figure 3 shows a photograph, an amplitude image, and a time of arrival image of a 25-mm-thick agarose block, which contained two 2-mm-thick silica colloid discs, 13 mm in diameter, made by mixing silica colloid with agarose, with one disc located 11 mm above the other and displaced in the Y direction. The time of arrival image was made by setting a threshold signal to yield a unit amplitude output, and discarding all signals with smaller amplitudes than the threshold. Note that the signal-to-noise ratio in the images could be improved significantly by employing an ultrasonic wave train with a higher duty cycle than the 0.2% duty cycle used here.

Experiments were also carried out to determine the magnitudes of vibration potentials from colloidal and ionic solutions, and biological samples. The apparatus shown in Fig. 1 was equipped with acrylic delay lines, and a 2.54-cm-diameter, planar pzt transducer driven by a single, negative voltage spike from a pulse generator (Panametrics, Inc. Model 5058PR). A number of common colloidal and ionic solutions[9] were shown to produce sizeable vibration potentials (given in parentheses), including colloidal gold (15 μV), India ink (44 μV), colloidal silver (13 μV), LiCl (6.9 μV), NaCl (23 μV), KCl (39 μV), RbCl (85 μV), and CsCl (132 μV). Insofar as tissue imaging is concerned,

muscle tissue from chicken breast, beef, and pork all produced vibration potentials smaller than 0.02 μV while whole blood,[10] which is both colloidal, as a result of the presence of red blood cells, and ionic, from dissolved electrolytes, gave comparatively large signals, on the order of 10 μV at 500 kHz. Further experiments with colloids placed between 4-mm-thick layers of chicken breast, with the breast tissue placed in contact with the electrodes, showed that vibration potential generated by the colloid within the weakly conducting muscle tissue is transmitted to the surface electrodes and can be recorded.

While the resolution in both vibration potential and conventional ultrasonic pulse-echo imaging are governed by the same principles of linear acoustics, the contrast mechanisms through which the images are formed in the two imaging methods are altogether different. In vibration potential imaging, contrast is determined by differences in electroacoustic properties within the irradiated body, i.e., by differences in the colloidal or ionic concentration or even the presence of such solutions, whereas in conventional ultrasonic pulse-echo imaging, contrast is determined by relative differences in acoustic impedance. In comparing vibration potential imaging with established methods such as optical or x-ray imaging, it is important to note that resolution is ultimately limited by the wavelength of the radiation employed.[11] An additional factor in considering the resolution of vibration potential imaging is that reflections of the acoustic waves at interfaces can cause changes in the vibration potential signal, complicating the analysis of data. Insofar as tissue imaging is concerned, the large difference in signal amplitudes between blood and muscle tissue found here, which is greater than a factor of 500, points up its contrast mechanism, which differs fundamentally from that for radiographic, photoacoustic, optical, or ultrasonic imaging, and which suggests its use, among other things, for detection of tumors, which are known to be highly vascularized.

[1] R. Zana and E. Yeager, in *Modern Aspects of Electrochemistry*, edited by J. O. Bockris, B. E. Conway, and R. E. White (Plenum, New York, 1982).
[2] R. J. Hunter, Colloids Surf., A **141**, 37 (1998).
[3] A. S. Dukhin and P. J. Goetz, Colloids Surf., A **192**, 267 (2001).
[4] We use Eq. (4.2) from R. W. O'Brien, J. Fluid Mech. **190**, 71 (1988).
[5] For a more complete description of vibration potential imaging in three dimensions see V. E. Gusev and G. J. Diebold (unpublished).
[6] The analysis here has ignored the effects of reflection of ultrasound at boundaries within the irradiated body.
[7] The colloidal silica Snow Tex (Nisson, Inc., Houston, TX) was an aqueous suspension of 20–30 nm silica with a particle concentration of 10^{15}/cm^3.
[8] The wave front in a focused sound beam has curvature which must be taken into account in a precise formulation of the problem.
[9] The colloidal gold (Ted Pella, Inc., Redding, CA) was an aqueous suspension of 100-nm-diam particles, at a concentration of 5×10^9/cm^3. India ink (Higgins, Inc., Levenburgh, TN) is an aqueous suspension of carbon with a surfactant added for stability. The colloidal silver was an aqueous suspension of 80-nm-diam particles, at a concentration of 1.1×10^{10}/cm^3. The salt concentrations were 4 M. Production of a vibration potential by these solutions is well known from previous reports in the literature.
[10] Whole canine blood preserved with EDTA.
[11] The resolution of nuclear magnetic resonance imaging is not determined by the wavelength of the radiation employed.

Acoustic radiation pressure: A "phase contrast" agent for x-ray phase contrast imaging

Claude J. Bailat,[a] Theron J. Hamilton, Christoph Rose-Petruck, and Gerald J. Diebold
Department of Chemistry, Brown University Providence, Rhode Island 02912

We show that the radiation pressure exerted by a beam of ultrasound can be used for contrast enhancement in high-resolution x-ray imaging of tissue and soft materials. Interfacial features of objects are highlighted as a result of both the displacement introduced by the ultrasound and the inherent sensitivity of x-ray phase contrast imaging to density variations. The potential of the method is demonstrated by imaging microscopic tumor phantoms embedded into tissue with a thickness typically presented in mammography. The detection limit of micrometer size masses exceeds the resolution of currently available mammography imaging systems. The directionality of the acoustic radiation force and its localization in space permits the imaging of ultrasound-selected tissue volumes. The results presented here suggest that the method may permit the detection of tumors in soft tissue in their early stage of development. © *2004 American Institute of Physics.*
[DOI: 10.1063/1.1818337]

Phase contrast imaging differs from conventional x-ray shadowgraphy in the mechanism of contrast generation: while conventional shadowgraphy depends on absorption of x rays, phase contrast imaging is based on phase changes as x rays traverse a body giving rise to wave interference that results in intensity changes in the image. Fresnel–Huygens theory,[1,2] which governs image formation in general, describes contrast in an image as dependent on both absorption and phase contrast. However, only when sources with high spatial coherence, such as synchrotrons,[3–5] microfocus x-ray tubes,[6,7] or laser plasma x-ray sources[8,9] are employed is the phase contrast component of the image visible. Coherent sources give an image of a dense object embedded in lower density, soft tissue as a shadow of the object, caused by absorption, surrounded at its perimeter by light and dark interference fringes arising from rapid phase variations in the radiation at the interface between the two media. A detailed analysis of the relative contrast produced in an image for a fixed difference in density shows that phase contrast is more sensitive than absorption throughout most of the spectral region commonly used for diagnostic x-ray imaging.[10] For instance, the thickness of water needed to produce a 1% phase-contrast at 36 keV photon energy is 2500 times smaller than that required to produce the same contrast though absorption.[10]

Phase contrast in an image can be markedly enhanced by recording two images of an object, one where the object is displaced slightly through acoustic radiation pressure,[11–13] and a second where the object is unmoved, followed by subtraction of the two images. Acoustic radiation forces[14–16] can arise from either reflection of sound by an object or as a result of acoustic impedance changes (i.e., a variation in either density or sound speed) or by dissipative processes within the object resulting in absorption of the ultrasound energy. A number of "elastographic" studies, where tissue movement is monitored in response to radiation or mechanical pressure,[11–13] have shown that variations in Young's modulus, which, in part, determines sound speed, permits acoustic differentiation of tissue. It is known, for instance,

that breast tumors have a significantly different Young's modulus from surrounding tissue, and that tumors move as rigid bodies in response to acoustic radiation pressure.[11–13,17,18]

The subtractive phase contrast imaging method described here is based on acoustic radiation pressure to generate differential movement of components of a body having variations in acoustic impedance. First, a reference x-ray phase-contrast image is taken with a CCD camera and stored in a computer; next, a second x-ray image is recorded while the body is irradiated with a directed beam of ultrasound, under the same imaging conditions as the reference image. By subtracting the two images, a difference image of the temporally averaged displacement induced by the ultrasound is obtained.

As shown in Fig. 1, x rays were generated by a microfocus x-ray tube (Oxford Instruments, model UB-M1), operated at 90 kV, which has a minimum source diameter of 25 μm as measured using a knife edge imaging procedure. The x rays were detected by a $Gd_2O_2S(Tb)$ fiber optic scintillation plate (Hamamatsu, Inc., model J6676) the fluorescence from which was imaged onto a liquid nitrogen cooled CCD camera (Roper Scientific model 7382-0001) interfaced to a computer. The source to detector distance was 2.6 m, while the sample to source distance was 35 cm, providing a magnification of 7.5. The x-ray beam exiting the sample propagated in a helium atmosphere in order to reduce x-ray
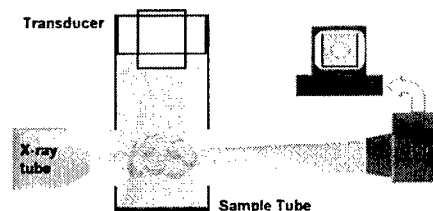

FIG. 1. Diagram of the experimental apparatus. X radiation generated by a microfocus tube penetrates a sample and is detected by a CCD camera that views a scintillator plate. The sample is located in a 3-cm-diam tube filled with water coupled to an ultrasound transducer. The intensity maximum in the x-ray spectrum detected at the scintillation screen was at 40 keV owing to x-ray spectrum hardening in the sample.
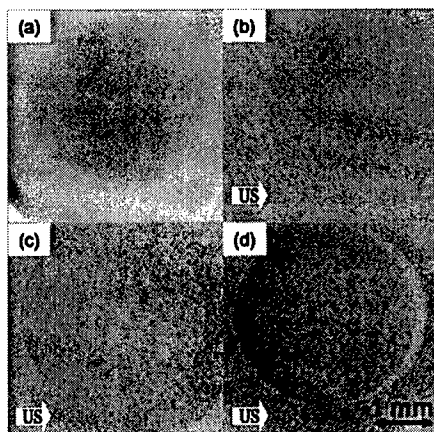
[a]Electronic mail: bailat@brown.edu

FIG. 2. (a) Conventional phase contrast image of a 3.05-mm-diam Teflon sphere suspended by a glass fiber in water showing both absorption and phase contrast. (b)–(d) Subtracted x-ray-acoustic phase contrast images taken with 10 kPa, 0.6 MPa, and 1.1 MPa average acoustic power applied to the transducer.

scatter. The sample was situated in the middle of a 3-cm -diam PVC tube which had portions machined out and replaced with Mylar. One end of the sample tube was terminated by a synthetic, sound-absorbing material while the other was sealed to a 2-cm-diam, 1 MHz, LiNb transducer, located 3 cm from the part of the sample traversed by the x-ray beam. The transducer was driven by a pulse train at a repetition rate of 133 Hz consisting of 15-μs-long 1 MHz bursts amplified by a power amplifier with a peak power of 1 kW.

The principle of the method was demonstrated by taking images of a 3 mm diameter Teflon™ bead attached to a glass fiber, suspended in water, and irradiated with pulsed ultrasound. A conventional phase contrast image showing both absorption and phase contrast at the perimeter of the bead is shown in Fig. 2(a). Figures 2(b)–2(d) show subtracted images taken over a range of successively higher acoustic powers. The absence of features in Fig. 2(b) shows that at the lowest acoustic intensity, the displacement of the bead is smaller than the resolution of the x-ray imaging apparatus. In Fig. 2(d) the displacement of the bead[19] with an acoustic pressure of 1.1 MPa was determined from the x-ray image to be 200 μm. Two effects from the subtraction of the image of the displaced bead from one of a stationary bead can be seen from examination of Fig. 2(c) and 2(d): first, the absorptive component of the contrast has been removed by the subtraction leaving only phase contrast in the image, and, second, the vector character of the image is evident in that interference fringes that lie parallel to the direction of the ultrasound induced motion are eliminated while those perpendicular to the direction of motion are highlighted.

The capability of the method for distinguishing only those objects irradiated with ultrasound was tested by imbedding two Teflon beads in agarose and directing a focused beam of ultrasound to irradiate only the bead nearest the x-ray source. Figures 3(a) and 3(b) show a conventional phase contrast image and an acoustically modulated phase contrast image, respectively. The ultrasound irradiated bead is easily identified with virtually no trace of the bead located outside the ultrasound field.

In order to evaluate the efficacy of applying the imaging method to tissue-like samples, the displacements of micron-sized pieces of agarose embedded in chicken breast were
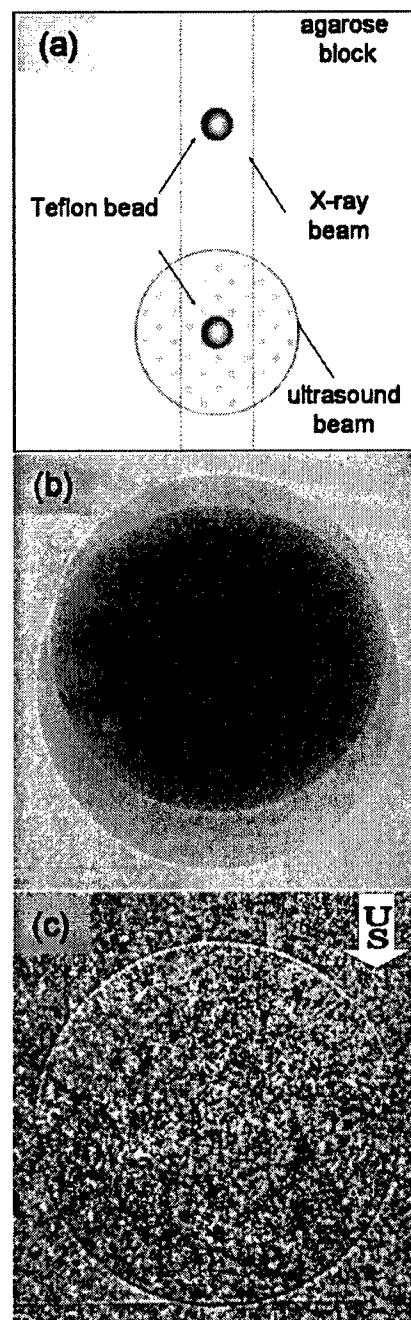

FIG. 3. (a) Top view of the sample consisting of two Teflon beads cast in agarose. The two beads are separated by 3 cm. (b) Conventional phase contrast image of two Teflon beads in agarose and (c) an acoustically modulated phase contrast image showing only the bead irradiated with ultrasound. The beads were located 2.5 cm apart.

measured. The agarose was enriched with carbon nanoparticles to achieve a density approximately 14% higher than that of the chicken breast in order to simulate the density difference between malignant and healthy human breast tissue.[20,21] Figure 4 shows a series of images of the chicken breast with the embedded objects. The flesh included fat globules which were deflected by the ultrasound field along with the agarose objects. All images contain identical detected x-ray doses and are reproduced with identical grey scale ranges of ±5% of the average image intensity. The images and inserts display the same sample regions around three selected agarose objects, labeled 1–3 with estimated sizes of 40×53 μm (1), 30×46 μm (2), and 20×26 μm
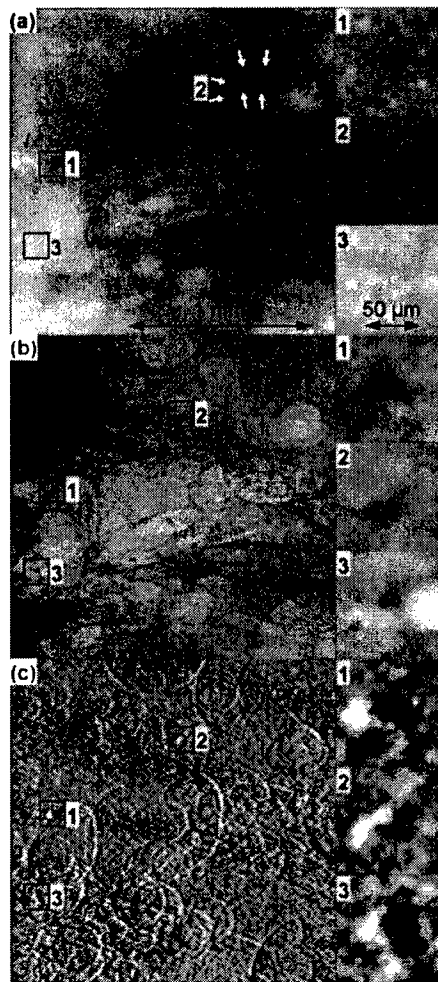
FIG. 4. X-ray images of carbon-enriched agarose objects embedded in chicken flesh: The round objects are fat globules in the chicken flesh. The entire sample is immersed in water. (a) X-ray image taken with an enlarged, 75-μm-diam x-ray source; (b) conventional phase contrast image taken with a 25-μm-diam x-ray source, and (c) x-ray ultrasound enhanced x-ray phase contrast image taken with 25-μm-diam x-ray source. Tissue regions that are not shifted by the ultrasound field are indicated by arrows. Inset: magnified images of objects 1–3. The background noise remaining after subtraction in image (c) is the shot noise.

(3). Figure 4(a) shows an image of the chicken breast where the x-ray spot size in the microfocus tube was deliberately enlarged to 75 μm. The phase contrast features of the image are almost entirely eliminated by convolution of the fringes over the spot size of the x-ray source—only the absorption component of the contrast remains in the image. Fatty material, which appears as nearly circular objects in the image, is visible but not well defined. Three different agarose pieces, referred to here as "objects," are in the field of view of the imaging system. While object 1 is visible, object 2 is poorly defined, and object 3 is essentially indistinguishable from the background. The overall visibility of the objects in the tissue is low. Figure 4(b) shows a conventional phase contrast image with the x-ray tube operating with its minimum source diameter, 25 μm. The image shows the fatty masses as being clearly outlined, permitting visual identification. Both objects 1 and 2 are visible, but object 3, again, is not easily distinguished from the background. The ultrasound contrast-enhanced x-ray image is shown in Fig. 4(c). The ultrasound intensity was adjusted to give a tissue displacement of ap-

proximately one x-ray diffraction fringe. Objects 1, 2, and 3 are clearly visible and are marked with identical shading, indicating motion in the same direction under the influence of the acoustic radiation pressure. The objects identified by arrows in Figs. 4(a)–4(c) are no longer visible in the image and can therefore be identified as either artifacts arising from optical imperfections in the sample container or imaging optics, or, as objects lying outside the ultrasonic field.

The salient feature of the acoustic contrast x-ray imaging described here is its ability to highlight density variations: both the x-ray phase contrast and the movement of the selected object respond to density variations. Inherent in the method is the rejection of all features, whether absorptive or refractive, from any object that does not respond to ultrasonic radiation pressure, or any object within a body that is not within the ultrasonic field. This feature gives the diagnostician the ability to address a specific region within a body with directed ultrasound and to obtain an x-ray image of that region only. Without a significant reduction in the resolution of the present imaging system of 2.5 μm/pixel at the object plane, a field of view of 10–15 cm in diameter is possible with current technology by using a larger imaging screen. The present results suggest application of the method to detection of small-sized tumors and other lesions distinguished from surrounding tissue by their elastic properties and density differences as small as a few percent.

[1]M. Born and E. Wolf, *Principles of Optics* (Pergamon, Oxford, 1980).
[2]J. M. Cowley, *Diffraction Physics* (North-Holland, Amsterdam, 1984).
[3]A. Snigirev, I. Snigireva, V. Kohn, S. Kuznetsov, and I. Schelokov, Rev. Sci. Instrum. **66**, 5486 (1995).
[4]F. Arfelli, V. Bonvicini, A. Bravin, G. Cantatore, E. Castelli et al., Phys. Med. Biol. **43**, 2845 (1998).
[5]A. Momose, Nucl. Instrum. Methods Phys. Res. A **352**, 622 (1995).
[6]A. Pogany, D. Gao, and S. W. Wilkins, Rev. Sci. Instrum. **68**, 2774 (1997).
[7]S. W. Wilkins, T. E. Gureyev, D. Gao, A. Pogany, and A. W. Stevenson, Nature (London) **384**, 335 (1996).
[8]A. Krol, A. Ikhjef, J. C. Kieffer, D. A. Bassano, C. C. Chamberlain, Z. Jiang, H. Pepin, and S. C. Prasad, Med. Phys. **24**, 725 (1997).
[9]A. Krol, J. C. Kieffer, and E. Forster, Proc. SPIE **3157**, 156 (1997).
[10]F. Beckmann, U. Bonse, F. Busch, and O. Gunnewig, J. Comput. Assist. Tomogr. **21**, 539 (1997).
[11]L. Gao, K. J. Parker, R. M. Lerner, and S. F. Levinson, Ultrasound Med. Biol. **22**, 959 (1996).
[12]K. Nightingale, R. Nightingale, M. Palmeri, and G. Trahey, IEEE Ultrasonics Symposium, 1999, p. 1319.
[13]K. Nightingale, D. Stutz, R. Bentley, and G. Trahey, IEEE Symposium, 2002, p. 525.
[14]P. Westervelt, J. Acoust. Soc. Am. **23**, 312 (1951).
[15]B. Chu and R. E. Apfel, J. Acoust. Soc. Am. **72**, 1673 (1982).
[16]R. T. Beyer, J. Acoust. Soc. Am. **63**, 1025 (1978).
[17]A. P. Sarvazyan, Ultrasound Med. Biol. **24**, 1419 (1998).
[18]S. A. McAleavey, IEEE Trans. Ultrason. Ferroelectr. Freq. Control **50**, 631 (2003).
[19]In separate experiments, it was determined that the movement of the bead was caused by acoustic radiation forces, and not streaming.
[20]F. A. Duck, *Physical Properties of Tissue* (Academic, London, 1990).
[21]P. C. Johns and M. J. Yaffe, Phys. Med. Biol. **32**, 675 (1987).

ELSEVIER

doi:10.1016/j.ultrasmedbio.2004.11.002

● *Original Contribution*

IMAGING WITH THE ULTRASONIC VIBRATION POTENTIAL: A THEORY FOR CURRENT GENERATION

VITALYI E. GUSEV* and GERALD J. DIEBOLD[†]

*Université du Maine, Le Mans, France; and [†]Department of Chemistry, Brown University, Providence, RI, USA

Abstract—The current in a circuit produced by a time-varying polarization generated by an object within a body in response to the passage of ultrasound (US) is found through solution to Maxwell's equations. Current generation is modelled in a body with uniform dielectric constant and conductivity where a finite region within the body produces an ultrasonic vibration potential. The results of the calculation form the mathematical basis for imaging through use of the ultrasonic vibration potential. (E-mail: Gerald_Diebold@brown.edu)   © 2005 World Federation for Ultrasound in Medicine & Biology.

Key Words: Ultrasound, Ultrasonic vibration potential, Imaging.

INTRODUCTION

The generation of a voltage in a colloidal or ionic suspension by ultrasound (US) is known as the ultrasonic vibration potential. In the case of a colloid, particles suspended within solution are charged and, in turn, are surrounded by a counter charge in the fluid giving the solution overall charge neutrality. Because the density of the particle and the surrounding fluid typically differ from each other, the passage of a sound through a suspension causes the motions of the particles and fluid to differ: in the typical case where the particles are denser than the surrounding fluid, the particles will execute a smaller amplitude motion than that of the fluid, with a phase that lags that of the fluid. The flow of the fluid relative to the particle distorts the normally spherical charge distribution of the counter charge and results in the creation of a dipole at the site of each particle, which alternates in direction on alternating cycles of the sound wave. If a pair of electrodes is placed in solution a distance one half of the sound wavelength apart, an alternating voltage can be recorded across the electrodes. The theory of the vibration potential, which was originally predicted by Debye (1933) for ionic solutions, has been reviewed by several authors

(Hunter 1998; Dukhin and Goetz 2001; Zana and Yeager 1983).

Here, we discuss the generation of the vibration potential as a means of imaging of colloidal or ionic species within an inert medium (Beveridge et al. 2004a, 2004b). The problem is to calculate the current developed in a pair of electrodes when US passes through a colloidal or ionic object within a body. The calculation for the Dirichelet problem is carried out for a pair of parallel electrodes at zero potential in contact with a medium with an isotropic conductivity and dielectric constant, within which is embedded an object with an arbitrary geometry of the same conductivity and dielectric constant as the surrounding medium, but which produces a vibration potential on the passage of US. There are two mechanisms for production of an alternating current in the circuit connecting the two electrodes: the first is the production of a current driven by the electric field in the body induced by the polarization, and the second is the generation of charges on the electrodes as a result of imposition of a time-varying polarization in the region between the parallel plates. This paper is divided into sections giving a derivation of Poisson's equation for determining the field from an arbitrary colloidal object, derivation of a Green's function for the parallel electrode geometry, and derivation of three expressions that can be used for calculating the current in an external circuit for an arbitrary object.

Address correspondence to: Dr. Gerald J. Diebold, Department of Chemistry, 324 Brook Street, Providence, RI 02912 USA. E-mail: Gerald_Diebold@brown.edu

POISSON'S EQUATION

The electric field $\mathbf{E}$ produced across a region of colloid by a pressure p, according to O'Brien (1988) is given by:

$$\mathbf{E} = \frac{f\Delta\rho_m\mu_E}{\rho_m\sigma^*}\nabla p, \qquad (1)$$

where f is the volume fraction of colloidal particles in the fluid, μ_E is the electrophoretic mobility of the particles, ρ_m is the mass density of the suspension and $\Delta\rho_m$ is the difference in densities between the particles and the surrounding fluid, and σ^* is the complex conductivity (O'Brien 1986; The complex conductivity σ^* used by O'Brien is a generalized conductivity that relates the current density to the electric field in a colloid).

Consider generation of the vibration potential in a medium with conductivity σ, and dielectric constant ε, assumed uniform throughout the medium under consideration, but with one region of the medium, referred to here as the object, that generates a vibration potential on the passage of sound. By combining the charge conservation relation $\nabla \cdot \mathbf{J} = \partial\rho/\partial t$, where $\mathbf{J}$ is the current density and ρ is the charge density, with the constitutive relation $\mathbf{J} = \sigma\mathbf{E}$, where $\mathbf{E}$ is the electric field and σ is the real part of the conductivity, and Maxwell's equation $\rho = \nabla \cdot \mathbf{D}$, where $\mathbf{D}$ is the electrical displacement, it follows that:

$$\nabla \cdot (\sigma\mathbf{E}) = -\frac{\partial}{\partial t}(\nabla \cdot \mathbf{D}). \qquad (2)$$

The effect of the passage of sound through the object, which is taken to be colloidal, is to produce an acoustic polarization $\mathbf{P}_a$ within the object, so that the displacement vector becomes:

$$\mathbf{D} = \varepsilon\mathbf{E} + \mathbf{P}_a, \qquad (3)$$

where ε is the dielectric constant of the object and the surrounding medium, assumed to be identical. It is assumed that the polarization $\mathbf{P}$ varies in space, depending on whether the coordinate is within the object or in the inert region of the body. The polarization produced by the sound, within the context of the present calculation, is taken to be:

$$\mathbf{P}_a = \alpha(\mathbf{x}, \omega)\nabla p \qquad (4)$$

where

$$\alpha(\mathbf{x}, \omega) = \varepsilon f\Delta\rho_m\mu_E/\rho_m\sigma^*.$$

The notation for $\alpha(\mathbf{x},\omega)$ explicitly contains the space variable to indicate that it takes on different values in the colloidal and non colloidal regions. The combination of eqn (3) with eqn (2) gives:

$$\nabla \cdot \left[\sigma\mathbf{E} + \frac{\partial}{\partial t}(\varepsilon\mathbf{E} + \mathbf{P}_a)\right] = 0. \qquad (5)$$

For the present problem, where the media under consideration would normally be biologic tissue, the frequencies where the vibration potential can be generated are restricted owing to ultrasonic absorption; hence, it is reasonable to make the quasi-electrostatic approximation where $\nabla \times \mathbf{E} \simeq 0$, so that the electric field can be written in terms of a potential ϕ as:

$$\mathbf{E} = -\nabla\phi. \qquad (6)$$

Substitution of eqn (6) into eqn (5) gives:

$$\sigma\Delta^2\phi + \varepsilon\frac{\partial}{\partial t}\nabla^2\phi = \frac{\partial}{\partial t}(\nabla \cdot \mathbf{P}_a), \qquad (7)$$

from which the potential in the time domain can be determined from a knowledge of $\mathbf{P}_a$ in space and time. Equation (7) can be found in the frequency domain by assuming that the acoustic pressure, the polarization and the potential vary sinusoidally in time according to:

$$p = \text{Re}[\tilde{p}(\mathbf{x})e^{i\omega t}]$$

$$\mathbf{P}_a = \text{Re}[\tilde{\mathbf{P}}_a(\mathbf{x})e^{i\omega t}]$$

$$\phi = \text{Re}[\tilde{\phi}(\mathbf{x})e^{i\omega t}],$$

which, on substitution into eqn (7), gives Poisson's equation for the frequency domain potential in terms of the acoustic polarization as:

$$\nabla^2\tilde{\phi} = \frac{i\omega}{\sigma + i\omega\varepsilon}\nabla \cdot \tilde{\mathbf{P}}_a, \qquad (8)$$

or

$$\nabla^2\tilde{\phi} = \nabla \cdot (\alpha^\dagger \nabla \tilde{p}), \qquad (9)$$

where $\alpha^\dagger$ is given by:

$$\alpha^\dagger(\mathbf{x},\omega) = \frac{i\omega}{\sigma + i\omega\varepsilon}\alpha(\mathbf{x}, \omega). \qquad (10)$$

It can be seen that eqns (8) and (9) are Poisson's equations with the acoustic polarization acting as a source. The source is dependent on derivatives of both the colloidal object and the pressure in space.

GREEN'S FUNCTION FOR THE POTENTIAL

Consider the geometry for imaging a colloidal object of arbitrary shape inside a weakly conducting body with a pair of conducting electrodes in contact with the external surface of the body, as shown in Fig. 1. The electrodes are considered to be parallel and spaced a distance h apart, with the direction of the US taken to be
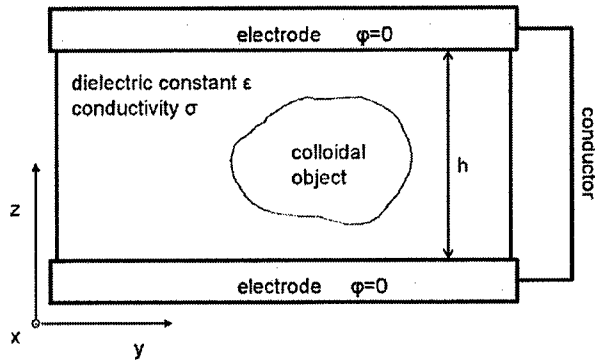
Fig. 1. A colloidal object is embedded within a body. The object and the surrounding region are taken to have a conductivity σ and a dielectric constant ε. Only the colloidal region within the body produces a vibration potential; the region outside the object is considered to be inert.

along the z-axis. The electrodes are assumed to be connected to each other through a conductor or, equivalently, through an amplifier with an input impedance of nearly zero so that the potentials of each of the electrodes are effectively zero. The potential $\tilde{\phi}$ within the body can be determined from a Green's function solution to Poisson's equation through use of a Dirichlet Green's function $G_D(\mathbf{x},\mathbf{x}')$, that satisfies the equation:

$$\nabla^2 G_D(\mathbf{x},\mathbf{x}') = \delta(\mathbf{x} - \mathbf{x}'), \qquad (11)$$

where $\mathbf{x}$ and $\mathbf{x}'$ are the field and source points, respectively. The potential, according to Green's theorem is then given by:

$$\tilde{\phi}(\mathbf{x}) = \int_{V'} G_D \nabla' \cdot (\alpha^\dagger \nabla' \bar{p}') dV' + \oint \left[\tilde{\phi} \frac{\partial G_D}{\partial n'} - G_D \frac{\partial \tilde{\phi}}{\partial n'} \right] dS', \qquad (12)$$

where the integration in both integrals is over the primed coordinates, and where the derivatives in the surface integral are taken with respect to the surface normal n. Because the potentials on the planes at $z = 0$ and $z = h$ are taken to be zero, it is convenient to construct a Green's function that is also zero on the surfaces of the electrodes and to take the surface of integration to be a rectangular enclosure in the body, with its ends at the positions of the electrodes where the potential is zero, and where the enclosure extends to infinity in the x and y directions.

Consider the Fourier transformation of the spatial coordinate in eqn (11) through the transform pair:

$$\bar{f}(\kappa_x, \kappa_y) = \frac{1}{(2\pi)^2} \int_{-\infty}^{\infty} \int_{-\infty}^{\infty} f(x,y) e^{-i(\kappa_x x + \kappa_y y)} dx dy \qquad (13a)$$

$$f(x,y) = \int_{-\infty}^{\infty} \int_{-\infty}^{\infty} \bar{f}(\kappa_x, \kappa_y) e^{i(\kappa_x x + \kappa_y y)} d\kappa_x d\kappa_y \qquad (13b)$$

to give the Green's function $\bar{G}_D(\kappa_x, \kappa_y, z; \mathbf{x}')$ in reciprocal space. Fourier transformation of eqn (11) gives:

$$\left(\frac{\partial^2}{\partial z^2} - \kappa_x^2 - \kappa_y^2 \right) \bar{G}_D(\kappa_x, \kappa_y, z; \mathbf{x}')$$

$$= \frac{1}{(2\pi)^2} \delta(z - z') e^{-i(\kappa_x x' + \kappa_y y')}, \qquad (14)$$

where the Green's function in reciprocal xy space is $\bar{G}_D(\kappa_x, \kappa_y, z)$. Because the Green's function must vanish at $z = 0$ and $z = h$, it can be of the form $\bar{G}_D = \Sigma A_m \sin(d_m z)$, where $d_m = m\pi/h$, A_m is a constant independent of z and m is an integer ranging from 1 to ∞. By multiplication of eqn (14) by $\sin d_{m'} z$ and integration of the resulting expression from 0 to h, it can be shown that the reciprocal space Green's function is given by:

$$\bar{G}_D(\kappa_x, \kappa_y, z; \mathbf{x}') = -\frac{1}{2\pi^2 h} \sum_{1}^{\infty} \frac{\left[\sin\left(\frac{m\pi}{h} z\right) \sin\left(\frac{m\pi}{h} z'\right) \right]}{\left[\left(\frac{m\pi}{h}\right)^2 + \kappa_x^2 + \kappa_y^2 \right]}$$

$$\times e^{-i\kappa_x x' - i\kappa_y y'}, \qquad (15)$$

which, on transformation back to coordinate space according to eqns (13a) and (13b) gives the Green's function as:

$$G_D(\mathbf{x},\mathbf{x}') = -\frac{1}{2\pi^2 h} \sum_{1}^{\infty} \sin\left(\frac{m\pi}{h} z\right) \sin\left(\frac{m\pi}{h} z'\right)$$

$$\times \int_{-\infty}^{\infty} \int_{-\infty}^{\infty} \frac{e^{i\kappa_x(x-x') + i\kappa_y(y-y')}}{\left[\left(\frac{m\pi}{h}\right)^2 + \kappa_x^2 + \kappa_y^2 \right]} d\kappa_x d\kappa_y. \qquad (16)$$

Because the potential $\tilde{\phi}$ is zero on the upper and lower electrodes by assumption, and $G_D(\mathbf{x}, \mathbf{x}')$ is zero on the upper and lower electrodes by construction, the surface integrals in eqn (12) are zero, so that the frequency domain potential is given by the volume integral:

$$\tilde{\phi}(\mathbf{x}) = \int_{V'} G_D(\mathbf{x},\mathbf{x}') \nabla' \cdot \left[\alpha^\dagger(\mathbf{x}', \omega) \nabla' \bar{p}(\mathbf{x}') \right] dV', \qquad (17)$$

where $G_D(\mathbf{x},\mathbf{x}')$ is given by eqn (16) and where the integration over the primed coordinates is explicitly indicated in the integrand.

THE CURRENT IN THE ELECTRODES

There are two mechanisms for production of current in the electrodes (O'Brien 1988). If the region between the two plates is a nonconducting dielectric, a current will be generated in the external circuit connecting the two electrodes as a result of the flow of charge induced by the time-varying polarization induced by the US in the colloidal or ionic object. The current density $\mathbf{J}_P$ generated by a time-varying displacement vector $\mathbf{D}$ is given by $\mathbf{J}_P = \partial \mathbf{D}/\partial t$, where the displacement vector can be found from the potential through eqn 6 and the constitutive relation for a dielectric $\mathbf{D} = \varepsilon \mathbf{E}$. Thus, $\mathbf{J}_P$ is found from the potential as

$$\mathbf{J}_p(\mathbf{x}) = -\varepsilon \frac{\partial}{\partial t} \nabla \phi(\mathbf{x}). \tag{18}$$

Similarly, when a field is produced in a weak conductor by a time-varying polarization, the current density for the free charge $\mathbf{J}_F$ is related to the electric field as $\mathbf{J}_F = \sigma \mathbf{E}$, so that the current density expressed in terms of the potential becomes:

$$\mathbf{J}_F(\mathbf{x}) = -\sigma \nabla \phi(\mathbf{x}), \tag{19}$$

The current produced by both mechanisms I is found by integrating the normal component of the electric field, that is, the component perpendicular to one of surfaces, over the surface of one of the electrodes S; hence, the expression for the frequency domain current $\tilde{I}$ in the external circuit is given by:

$$\tilde{I} = \frac{(\sigma + i\omega\varepsilon)}{2\pi^2 h} \int \int_{S'} dxdy \int_{V'} \frac{\partial}{\partial z} G_D(\mathbf{x}, \mathbf{x}')\Big|_{z=0}$$

$$\nabla'$$

$$\cdot \left[\alpha^\dagger(\mathbf{x}', \omega) \nabla' \tilde{p}(\mathbf{x}') \right] d$$

$$V',$$

which, on substitution of $G_D(\mathbf{x}, \mathbf{x}')$ from eqn (16) carrying out the differentiation with respect to z, and evaluation of the integral at $z = 0$ gives:

$$\tilde{I} = \frac{(\sigma + i\omega\varepsilon)}{2\pi^2 h} \int \int_{S'} dxdy \int_{V'} \sum_1^\infty \left(\frac{m\pi}{h}\right) \sin\left(\frac{m\pi}{h}z'\right)$$

$$\times \int_{-\infty}^{\infty} \int_{-\infty}^{\infty} \frac{e^{i\kappa_x(x-x')+i\kappa_y(y-y')}}{\left[\left(\frac{m\pi}{h}\right)^2 + \kappa_x^2 + \kappa_y^2\right]} d\kappa_x d\kappa_y \nabla'$$

$$\cdot \left[\alpha^\dagger(\mathbf{x}', \omega) \nabla' \tilde{p}(\mathbf{x}') \right] d$$

$$V'. \tag{20}$$

Note that the factor of $(\sigma + i\omega\varepsilon)$ appears both in the prefactor to the integral and in the denominator of eqn (10) that defines $\alpha^\dagger$; hence, eqn (20) can be expressed in terms of α rather than $\alpha^\dagger$. The integration over x and y gives $(2\pi)^2 \delta(\kappa_x)\delta(\kappa_y)$, which simplifies eqn (20) considerably. Through use of the identity:

$$\sum_1^\infty \frac{\sin nx}{n}(-1)^n = -\frac{1}{2}x$$

eqn 20a can be shown to reduce to:

$$\tilde{I} = -\frac{i\omega}{h} \int_V z \left[\frac{\partial}{\partial x}\left(\alpha \frac{\partial}{\partial x}\tilde{p}\right) \right.$$

$$\left. + \frac{\partial}{\partial y}\left(\alpha \frac{\partial}{\partial y}\tilde{p}\right) + \frac{\partial}{\partial z}\left(\alpha \frac{\partial}{\partial z}\tilde{p}\right) \right] dxdydz, \tag{21}$$

where the primes have been dropped in the integrand. If each of the terms in eqn (21) is integrated by parts, noting that the dimensions of the object are such that it does not contact either of the electrodes, so that α can be taken as zero at $z = h$ or $z = 0$, it is not difficult to show that the only term that remains is the third term in the integrand, so that the current is given by:

$$\tilde{I} = \frac{i\omega}{h} \int_V \alpha(\mathbf{x}, \omega) \frac{\partial}{\partial z} p(\mathbf{x}) dxdydz. \tag{22}$$

It is also possible to carry out an integration of this expression by parts as well, giving an alternate expression for the current in the circuit as:

$$\tilde{I} = -\frac{i\omega}{h} \int_V \left[\nabla \alpha(\mathbf{x}, \omega) \right]_z p(\mathbf{x}) dxdydz. \tag{23}$$

A useful integral can be derived from eqn (22) by using the linearized Navier–Stokes law for an inviscid fluid, $\nabla p/\rho = -\ddot{\mathbf{u}}$ where $\mathbf{u}$ is the displacement of the medium in the acoustic field. The acceleration in a plane wave can be expressed in terms of the displacement through the relation $\ddot{\mathbf{u}} = -\omega^2 \mathbf{u}$. Thus, an expression for the current in terms of the displacement in the plane wave can be written as:

$$\tilde{I} = \frac{i\rho\omega^3}{h} \int_V \alpha(\mathbf{x}, \omega) \tilde{u}(\mathbf{x}) dxdydz. \tag{24}$$

INFINITE SLAB

The problem of a slab of thickness a located between two metal electrodes connected by a low-impedance amplifier, as shown in Fig. 2, can be solved by application of eqn (23). The impedance of the amplifier is taken to be so small that it acts as a short circuit, so that the potential of the two electrodes can be considered as
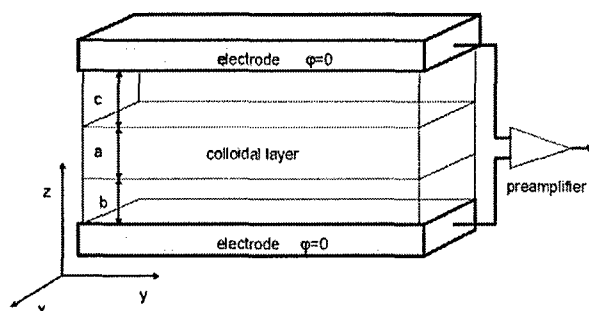
Fig. 2. An infinite slab of a colloidal suspension lies between two electrodes. The input impedance of the amplifier is considered to be sufficiently low that the potential of each electrode can be taken to be zero.

zero. The slab and the surrounding material are considered to have the same dielectric constant ε; however, the slab in region "a", located between $z = b$ and $z = b + a$ is assumed to be the only region where a vibration potential is generated. The ultrasonic beam is assumed to be continuous and to propagate along the positive z-axis. For the present problem, the distribution of colloid in space is given by $\alpha(z,\omega) = \alpha_0[u(z - b) - u(z - b - a)]$, where α_0 refers to a value of $\alpha(x,\omega)$ independent of x in layer a whose magnitude is given by eqn (4), and u is the Heaviside function. Because the layers are considered to be infinite in the x and y directions, a current per unit area J is generated by the time-varying polarization, which, according to eqn (23), is found to be:

$$\tilde{J} = -\frac{i\omega\alpha_0}{h}\left[\tilde{p}(b + a) - \tilde{p}(b)\right].\qquad(25)$$

It is possible to consider the same problem without the use of eqn (23) by assuming a time-varying polarization $\mathbf{P}_a$ that is generated by the vibration potential, and calculating the resulting current when the material in layers "b" and "c" are dielectrics with dielectric constant ε. From eqn (3a), the electric field in the three regions is given by:

$$E(z) = \frac{1}{\varepsilon}\left[D_0 - P_a(z)\right],\qquad(26)$$

where E, D and P_a are the components of electric field, displacement, and acoustic polarization along the positive z-axis. The acoustic polarization has a value P_a inside region a, and is zero in regions b and c. Because there are no free charges in the three layers, the displacement vector has a constant value D_0. From eqn (6), it follows that:

$$\phi(h) - \phi(0) = 0 = -\int_0^h E dz = \frac{-1}{\varepsilon}\left[\int_0^h D_0 dz\right.$$
$$\left. -\int_b^{a+b} P_a dz\right].\qquad(27)$$

Therefore, the component of the displacement vector along the z-axis in all three layers is given by:

$$D_0 = \frac{1}{h}\int_b^{b+a} P_a dz.\qquad(28)$$

It is not difficult to show that the electric fields and polarizations in regions b and c are identical. If an integration volume is taken as a closed cylindrical volume crossing the region between the upper electrode and region b, then it follows from Maxwell's equation $\nabla \cdot \mathbf{D} = \rho$ that $D_0 = -\sigma_s$, where σ_s is the charge density on the upper electrode. Because magnitude of the current density J is given by $J = d\sigma_s/dt$, the frequency domain current density is:

$$\tilde{J} = -\frac{i\omega}{h}\int_b^{b+a} P_a dz,\qquad(29)$$

which, for an acoustic polarization $\tilde{\mathbf{P}}_a = \alpha(\omega, \mathbf{x})\nabla\tilde{p}$, recovers eqn (25), as found directly from eqn (23), above.

Note the simplification that follows from the assumption of a 1-D geometry in this problem. If an acoustic beam with a finite cross-section were employed, then the direction of the electric field would not be parallel to the z-axis over the entire area of the slab, and a more complicated calculation of the current density would be required. The magnitude of the error in determining the current density through use of eqn (25) for a finite cross-section acoustic beam would, of course, depend on the dimensions of the beam relative to the width of the gaps between the colloidal layer and the conductors.

DISCUSSION

Equations (22) to (24) give three equivalent expressions for the current in a circuit generated by a colloidal or ionic object inside a body irradiated by a beam of US. The third of these gives perhaps the most intuitive picture of the process of current generation, in that it states that the current is proportional to material displacement in the acoustic wave integrated over the region where colloid is present. Thus, the production of current is seen as proportional to the integration of the dipole moments at the sites of the particles over the region where there is a displacement caused by the acoustic wave. Note that, depending on the frequency and spatial extent of the wave, the integration can be finite or zero. This property

is seen explicitly in the solution for the current given by eqn (25), which shows that a sinusoidal pressure wave whose spatial extent is smaller than the length of the colloidal region generates no signal when the wave is confined within the colloidal layer (in which case $\bar{p}(b + a) = \bar{p}(b) = 0$); only when such a short burst enters or exits the layer is a current produced. For a continuous wave, or an ultrasonic burst whose spatial extent is large compared with the layer thickness, when an even or odd number of half wavelengths of the acoustic wave equals the length of the colloidal layer, the vibration potential across the layer integrates to zero, or takes on a maximal value. For other wavelengths, the signal integrates to some current intermediate between these two extrema. Further, it is easy to see that recording the frequencies that give consecutive maxima and minima in the vibration potential permits determination of the layer thickness. The simple example of the slab also makes clear the interpretation of eqn (23), in that a gradient of the concentration of colloid is required for a current to be generated for burst of US: a fixed amplitude sound wave crossing a boundary between colloidal and inert material generates a current at the points where it enters or leaves the colloidal region. Equally, eqn (22) states that, if there is an acoustic wave that varies in space propagating wholly within a colloidal layer of uniform concentration, it is possible to observe a current from the vibration potential.

Different methods of generating an image are evident in the results obtained here. In addition to determination of the thickness of a colloidal or ionic layer in a 1-D geometry already mentioned, a method based on the time of appearance of the vibration potential is inherent in eqns (23) and (24). The distance a colloidal region lies from the launching point of an ultrasonic wave can be determined from a knowledge of the sound speed in the body and the appearance time of the vibration potential signal relative to the launching time of the sound wave,

in a manner analogous to conventional ultrasonic imaging. In general, the frequency-dependence of the current for a continuous ultrasonic wave, or the time-dependence of any acoustic burst sequence generated by an object whose geometry is known, can be determined from eqn (23). It is expected that, for a number of simple geometries, straightforward expressions for the vibration potential can be obtained in closed from, which will prove of value in the interpretation of vibration potential signals for imaging (Beveridge et al. 2004b). In summary, the present work gives explicit expressions for the current recorded in an imaging experiment for objects whose geometry is known *a priori*; in addition, it gives a starting point for solution of the inverse problem where vibration potential data are gathered to determine the spatial extent of an arbitrary object whose geometry and location within a body is sought.

REFERENCES

Beveridge AC, Wang S, Diebold GJ. Vibration potential imaging: Theory and preliminary results. Proc SPIE 2004a;5320:95–100.

Beveridge AC, Wang S, Diebold GJ. Imaging based on the ultrasonic vibration potential. Appl Phys Lett 2004;85:5466–5468.

Debye PJJ. A method for determination of the mass of electrolytic ions. Chem Phys 1933;1:13–16.

Dukhin AS, Goetz PJ. New developments in acoustic and electroacoustic spectroscopy for characterizing concentrated dispersions. Colloids Surfaces A 2001;192:267–306.

Hunter RJ. Recent developments in the electroacoustic characterization of colloidal suspensions and emulsions. Colloids Surfaces 1998; 141:37–66.

O'Brien RWJ. The high frequency dielectric dispersion of a colloid. Colloid Interface Sci 1986;113:81–93.

O'Brien RWJ. Electro-acoustic effects in a dilute suspension of spherical particles. Fluid Mech 1988;190:71–86.

Zana R, Yeager E. Ultrasonic vibration potentials. In: Bockris JO'M, Conway BE, White RE, eds. Modern aspects of electrochemistry. New York: Plenum, 1983:1–60.

Acoustically modulated x-ray phase contrast imaging

**Theron J Hamilton, Claude J Bailat, Christoph Rose-Petruck
and Gerald J Diebold**

Department of Chemistry, Box H, Brown University, Providence, RI 02912, USA

Abstract
We report the use of ultrasonic radiation pressure with phase contrast x-ray imaging to give an image proportional to the space derivative of a conventional phase contrast image in the direction of propagation of an ultrasonic beam. Intense ultrasound is used to exert forces on objects within a body giving displacements of the order of tens to hundreds of microns. Subtraction of images made with and without the ultrasound field gives an image that removes low spatial frequency features and highlights high frequency features. The method acts as an acoustic 'contrast agent' for phase contrast x-ray imaging, which in soft tissue acts to highlight small density changes.

1. Introduction

When an x-ray beam traverses a body the spatial intensity profile of the beam is modified by the effects of absorption, scattering and phase changes, all of which depend essentially on the density of electrons. The first two of these effects form the basis of conventional radiography where a shadow is produced in the image wherever an object is of higher density than its surroundings. A second contrast mechanism, known as phase contrast, follows directly from the Huygens–Fresnel plane-wave theory of image formation, which responds to changes in index of refraction. The effect of phase contrast is subtle and is seen only when a spatially coherent source of x-rays is employed. The Fresnel–Kirchhoff integral (Born and Wolf 1980, Cowley 1984) for one dimension in the image plane x, gives the field amplitude $f(x)$ of the x-ray beam at a distance z from the object as

$$f(x, z) = \left(\frac{i}{\lambda z}\right)^{1/2} \exp(-ikz) \int q(X) \exp\left(\frac{-ik(x - X)^2}{2z}\right) dX \qquad (1)$$

where γ is the wavelength of the radiation, k is the wave number of the radiation and $q(X)$ describes the transmission of the object. The transmission function, $q(x)$, for an object gives the effect of the object on both the phase and the amplitude of the incoming wave

and determines the intensity pattern in the image. For a thin object with a small integrated absorption, $q(x)$ can be written as

$$q(x) = \exp(i\phi(x) - \mu(x)) \tag{2}$$

where φ and μ describe the change in phase and amplitude of the incoming wave, respectively, in passing through the object. The intensity of the image $I(x) = |f(x)|^2$ for a weak phase object can be shown to be

$$I(x) = 1 - \frac{\lambda z}{2\pi}\phi''(x). \tag{3}$$

Similarly, for a weak absorber, the intensity at the image plane is given by

$$I(x) = 1 - 2\mu(x). \tag{4}$$

In a typical phase contrast image of an object embedded in a lower density medium, the usual shadowgraph from absorption is present according to equation (4), but at the edges of the object interference fringes are observed. According to equation (3), which is valid for low spatial frequencies, the intensity in the image varies as the second derivative of the phase variation in the object, which tends to be greatest for smooth objects at the interface between the object and the surrounding medium.

Several techniques have been used to record phase variations. In electron microscopy, for example, phase contrast is obtained by defocusing the electron beam and is imaged on a scintillation screen. X-ray sources with high spatial coherence, such as synchrotrons (Snigirev *et al* 1995, Fulvia Arfelli *et al* 2000, Momose 1995), microfocus x-ray tubes (Pogany *et al* 1997, Wilkins *et al* 1996) or laser plasma x-ray sources (Krol *et al* 1997a, 1997b) are commonly used for phase contrast imaging.

A detailed analysis of the relative contrast produced in an image for a fixed difference in density shows that the phase contrast is more sensitive than the absorption for detection of density differences throughout most of the spectral region commonly used for diagnostic x-ray imaging (Beckmann *et al* 1997). For instance, the thickness of water needed to produce a 1% phase contrast at 36 keV photon energy is 2500 times smaller than that required to produce the same absorption contrast (Beckmann *et al* 1997). As a consequence, x-radiation with a high photon energy, which is only weakly absorbed, can be used in phase contrast imaging to obtain the same sensitivity to density change as much more strongly absorbed, low energy x-radiation used in absorption imaging, the obvious advantage of the former being a far lower dose of absorbed radiation in the irradiated material. The size of the smallest phase object (i.e. an object where $\mu = 0$) that can be detected by phase contrast can be estimated for an object, with index of refraction δ_{object}, embedded in a surrounding medium, with index of refraction δ_{medium}, from the relation

$$\Phi_{1\%} = \frac{2\pi t_{1\%}}{\lambda}(\delta_{\text{object}} - \delta_{\text{medium}}) \tag{5}$$

where $t_{1\%}$ is the thickness of the object required to produce an intensity change of 1%, corresponding to a phase change of 0.14 rad. Consider application of equation (5) to tumour detection in soft tissue. Several studies (Johns and Yaffe 1987, Duck 1990) have determined that mass density differences between malignant, for instance infiltrating carcinomas, and healthy breast tissue are of the order of 10% (Duck 1990, Johns and Yaffe 1987). Since δ is approximately 10^{-6} for soft tissue, the quantity $\delta_{\text{object}} - \delta_{\text{medium}}$ is of the order of 10^{-7}. At an x-ray energy of 40 keV, corresponding to a wavelength of 31 pm, equation (5) gives $t_{1\%}$ as 7 μm, which implies that, ignoring specific morphological features, malignant tissue with a thickness of about 10 μm can be distinguished from benign tissue assuming a signal-to-noise

ratio of at least 100. For the results discussed in this paper, the signal-to-noise ratio is 15, which is sufficient to distinguish object with a thickness of at least 45 μm.

Here we report experiments where pulsed ultrasound is used to create displacements of objects within water and soft tissue. The displacement of objects with densities different from that of the surrounding body is used to modify a phase contrast x-ray giving an image with an enhanced phase contrast component. Section 2 gives calculations of the radiation pressure on spheres useful for predicting displacements of spherical objects by ultrasound. Section 3 describes the x-ray apparatus and experiments where displacements of the order of microns were produced by acoustic radiation pressure (Westervelt 1951, Chu and Apfel 1982, Beyer 1978) and measured phase contrast radiographically. Section 4 describes the x-ray acoustic method of image formation and gives examples of its use. The discussion section comments on some of the features of the method and discusses applications.

2. Acoustic radiation pressure

Acoustic radiation forces arise from two processes, either reflection of sound by an object as a result of an acoustic impedance change (i.e., a variation in either density or sound speed) or by absorption of sound by the object. A number of studies (Muthupillai *et al* 1995, Gao *et al* 1996, Fatemi and Greenleaf 1998, Nightingale *et al* 1999, Sarvazyan 1998, McAleavey 2003) have shown that the soft tissue can be manipulated by ultrasound pressure. Typically, a mechanical actuator or a beam of ultrasound moves an object whose position is monitored in time with conventional pulse-echo ultrasonic imaging. It has been shown that variations in Young's modulus, which, in part, determines sound speed, permit acoustic differentiation of tissue. It is known, for instance, that breast tumours have a significantly different Young's modulus from surrounding tissue, and that tumours move as rigid bodies in response to acoustic radiation pressure (Gao *et al* 1996, Nightingale *et al* 1999, 2002, Sarvazyan 1998, McAleavey 2003). It should also be noted that, at least in a mammographic application, the collective motion associated with respiration and blood pressure is minimized by immobilizing the breast.

For the purposes of the present study, where reflection of the acoustic wave is considered, it can be said that for a fixed acoustic impedance change, the force exerted by an ultrasonic wave is proportional to the time average of the energy density of the wave and the area of the object presented to the sound field. An expression for the acoustic radiation force on an arbitrary object has been given by Westervelt (1951) and evaluated for spheres small compared with the wavelength of the radiation. For spheres of any diameter, King (1934) has given an expression that agrees with the limiting expression given by Westervelt. According to King, the average acoustic radiation force exerted on a sphere of radius a is given by:

$$\bar{F}_{\text{ac}} = \frac{2\pi p^2}{(ka)^2 k^2 c^2 \rho} A(ka) \tag{6}$$

where ρ and c are the density and the speed of sound of the medium, respectively, p is the acoustic pressure, k is the wave number of the radiation, and $A(ka)$ is given by

$$A(ka) = \frac{1}{H_0 H_1} + \frac{2}{H_1 H_2} \left\{ \frac{\left[(ka)^2 - 3\left(1 - \frac{\rho}{\rho_s}\right)\right]^2}{(ka)^8} \right\} + \sum_{n=2}^{\infty} \left(\frac{(n+1)}{H_n H_{n+1}} \frac{((ka)^2 - n(n+1))^2}{(ka)^{4(n+1)}} \right) \tag{7}$$

where the functions H_n for small ka are given by

$n = 0$:

$$H_0 = \frac{(1 + (ka)^2)}{(ka)^2}$$

$n = 1$:

$$H_1 = \frac{4}{(ka)^6} \left(\left(1 + \frac{\rho}{2\rho_s}\right)^2 + \frac{(ka)^2}{2} \left(1 + \frac{\rho}{2\rho_s}\right)^2 \frac{\rho}{\rho_s} + \frac{(ka)^4}{4} \right)$$

$n = 2$:

$$H_2 = \frac{81}{(ka)^{10}} \left(1 + \frac{(ka)^2}{10} - \frac{2(ka)^2}{81} + \frac{(ka)^6}{81} \right)$$

$n > 2$:

$$H_n = \frac{(n+1)^2 \left(\prod_{i=1}^{n} (2n-1)\right)^2}{(ka)^{4n+2}} \left(1 + \frac{n-1}{(n+1)(2n-1)}(ka)^2 + \cdots \right)$$

where ρ is the density of the fluid and ρ_s is the density of the sphere. For $ka > 2$, the functions H_n are given by

$n = 0$:

$$H_0 = \frac{(1 + (ka)^2)}{(ka)^2}$$

$n = 1$:

$$H_1 = \frac{\pi}{2(ka)^3} \left(\left(1 - \frac{\rho}{\rho_s}\right)^2 \left(J_{\frac{3}{2}}^2 + J_{-\frac{3}{2}}^2\right) + 2ka \left(1 - \frac{\rho}{\rho_s}\right)\left(J_{-\frac{3}{2}} J_{-\frac{5}{2}} + J_{\frac{3}{2}} J_{\frac{5}{2}}\right) + (ka)^2 \left(J_{\frac{5}{2}}^2 + J_{-\frac{5}{2}}^2\right) \right)$$

$n > 1$:

$$H_n = \frac{\pi}{2(ka)^{2n+1}} \left(n^2 \left(J_{n+\frac{1}{2}}^2 + J_{-n-\frac{1}{2}}^2\right) + 2ka \left(J_{-n-\frac{1}{2}} J_{-n-\frac{3}{2}} + J_{n+\frac{1}{2}} J_{n+\frac{3}{2}}\right) + (ka)^2 \left(J_{n+\frac{3}{2}}^2 + J_{-n-\frac{3}{2}}^2\right) \right)$$

where J_n is a Bessel function of order n, and where the argument of each of the Bessel functions is ka.

Figure 1 is a plot of force versus ka from equation (7), with the inset showing a portion of the curve for small ka. The parameters used in equation (7) were for a Teflon bead with $a = 1.5$ mm, $\rho/\rho_s = 2$; and for water with $c = 1500$ m s^{-1} and $\rho = 10^3$ kg m^{-3}. The curves in figure 1 show, unlike optical radiation forces, a steady increase in the force with increasing ka; the acoustic radiation pressure, of course, has a much weaker dependence on ka.

3. Radiation force experiments

Experiments were carried out to determine the deflection of a Teflon bead in water using an x-ray imaging apparatus to determine the deflection of the bead as a function of acoustic pressure. The x-rays, generated by a microfocus x-ray tube (Oxford Ultrabright Microfocus UB-M1), were directed onto a sample cell consisting of a 3 cm diameter PVC tube which had portions machined out and replaced with Mylar foil to reduce x-ray intensity losses. The x-ray beam, as shown in figure 2, propagated through a He filled tube to a Gd_2O_2S(Tb) fibre optic scintillation plate (Hamamatsu, Inc. Model J6676) the fluorescence from which was imaged onto a liquid nitrogen cooled CCD camera (Roper Scientific Model 7382-0001). The intensity
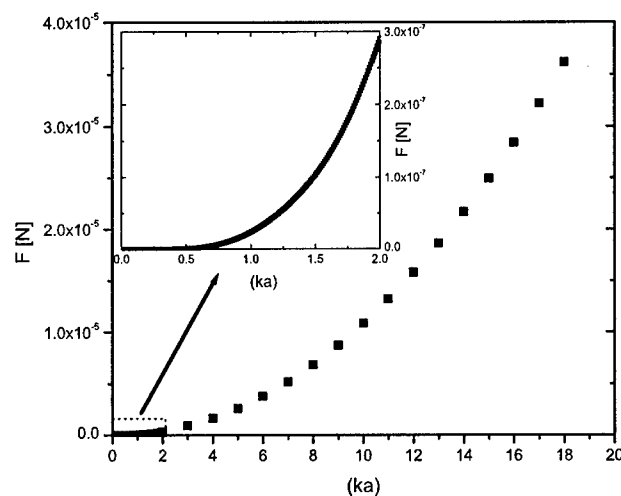
Figure 1. Radiation force (in N) versus ka (dimensionless) from equation (6). Inset: magnified view of the first part of the curve. The portions of the curves for $ka < 2$ were calculated using the small ka expressions for the functions H_n.
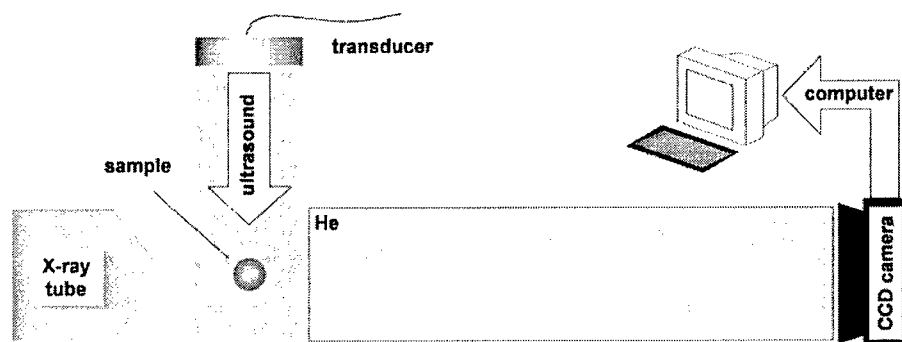
Figure 2. Diagram of the experimental apparatus. X-radiation generated by a microfocus tube penetrates a sample and is detected by a CCD camera that views a scintillation plate. The CCD camera is read by the computer which stores the images and performs the subtractions.

maximum of the emission x-ray spectrum was 40 keV. The source-to-detector distance was 2.6 m, while the sample-to-source distance was 0.35 m, giving a magnification of 7.5 and a maximum phase contrast (Pogany et al 1997) for spatial frequencies corresponding to 4.3 μm.

The acoustic transducer used to produce radiation pressure was a 1 MHz, LiNbO$_3$-transducer located 3 cm from the bead. One end of the PVC sample tube was terminated by a synthetic, sound-absorbing plastic. The pulse train from the function generator (Agilent Model 33250A) used to drive the transducer consisted of 15 μs bursts at a repetition rate of 133 Hz. The signal from the function generator was amplified by a power amplifier with a peak output power of 1.5 kW and delivered to the transducer. Although the low duty cycle of the pulse sequence, approximately 0.2%, resulted in a reduced time average acoustic power from the transducer, the resulting radiation pressure was sufficient to cause displacements that could be easily imaged with the CCD camera.
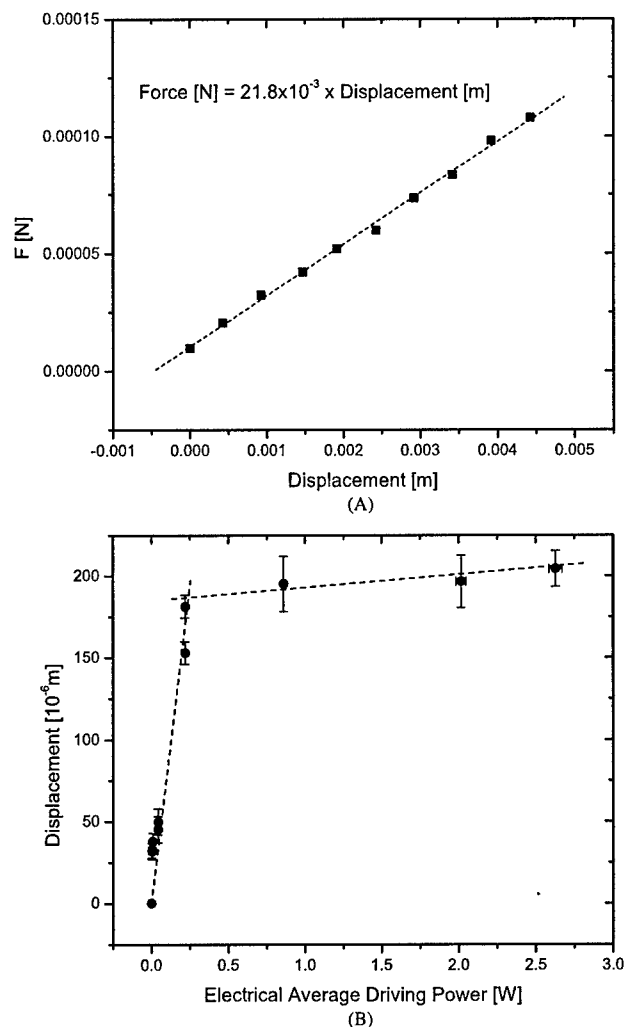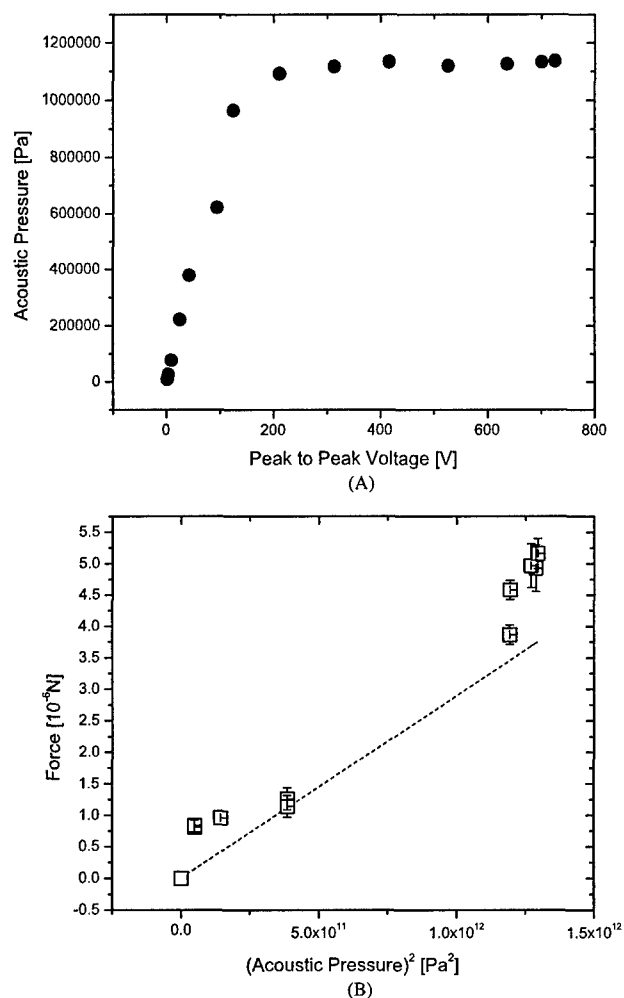
Figure 3. (A) Force on the glass fibre in N versus displacement in m. (B) Displacement of the Teflon bead attached to the fibre versus average electrical power delivered to the transducer.

A 3 mm diameter Teflon bead was attached to a glass fibre and suspended at the centre of the sample cell, which was filled with water. The glass fibre was calibrated by attaching it to a precision translation stage and using a laboratory balance to determine force versus fibre displacement. The data shown in figure 3(A) gave a force constant of 2.18×10^{-2} N m^{-1} for the fibre. The total force on a bead suspended from the fibre is the sum of the restoring force from the fibre and the force from gravity, which can be written for small angles of deviation from the vertical as

$$F_{\text{exp}} = F_{\text{glassfibre}} + \frac{m_{\text{bead}}\, g d}{L} \tag{8}$$

where m_{bead} is the mass of the bead, g is the gravitational constant, L is the length of the fibre and d is its displacement. For the experiments described here, the mass of the bead was

Figure 4. (A) Acoustic pressure in Pa from the calibrated transducer versus driving voltage from the power amplifier. (B) Force on the bead in N versus the square of the pressure from the transducer.

35 mg, and the length of the glass fibre was 10 cm. The displacement of the bead versus the time averaged electrical power delivered to the transducer is shown in figure 3(B). The break in the slope of the curve can be attributed to a departure of the efficiency of the transducer from linearity at high driving voltages. The acoustic pressure generated by the transducer at various power levels from the power amplifier was determined using a calibrated $LiNiO_3$ transducer (LaserSonics Technologies, Model WAT-04). The plot of acoustic pressure from the calibrated transducer versus average driving voltage applied to the transducer is shown in figure 4(A) which gives a curve with the same qualitative features as the curve in figure 3(B), and permits calibration of the transducer pressure in terms of the power amplifier output driving voltage. With this calibration, the plot in figure 3(B) can be converted to a plot of force versus the square of the acoustic pressure as shown in figure 4(B). The theoretical curve

from equation (6), also plotted in figure 4(B), shows reasonably good agreement with the experimental measurements. The maximum force recorded in the experiments was 5 μN.

4. Acoustically modulated x-ray phase contrast images

The method of modifying a phase contrast image using acoustic radiation pressure (Bailat *et al* 2004) consists of two steps: first, an x-ray image is made with a sound beam directed into a body to displace an object through acoustic radiation force and the image stored in a computer, second, another x-ray image of the object is taken, this time without the presence of the sound beam and the image is recorded in the computer. The two images are then subtracted pixel by pixel to give a subtracted phase contrast image, the component of the image from absorption contrast being largely eliminated, leaving a nearly pure phase contrast image, inherently background and flatfield corrected.

The principle of the method was demonstrated by taking images of two 3 mm diameter Teflon beads cast in a 6.5 cm long block of agarose. As shown in figure 5(A), the two beads were both within the field of the x-ray beam, but only one bead was irradiated with ultrasound. Figure 5(B) shows an image of the two beads where the microfocus x-ray tube was operated at high power, 80 W, to enlarge the diameter of the x-ray source to approximately 75 μm. With this source diameter, the phase contrast component of the image disappears as a result of convolution of the phase contrast fringes over the source area of the x-ray beam. The exposure time for the image was 75 s. In figure 5(C) a conventional phase contrast image of the two beads is shown using the same total x-ray fluence as was used in figure 5(B), but with the x-ray tube operating at 10 W, where the source diameter was 25 μm. The fringes at the perimeters of the beads, which serve to define the edges of the beads, are the result of interference from rapid phase variations in the x-ray paths, which, for a sphere, are largest at its perimeter (Wilkins *et al* 1996). The results of the image subtraction with the ultrasound directed onto only the bead closest to the x-ray tube are shown in figure 5(D). The bead that was not irradiated with ultrasound is not visible in the image, while the phase contrast component of the image of the irradiated bead shows up with the phase contrast component highlighted. The subtracted phase contrast image in figure 5(D) shows a reversal of the bright and dark regions at the perimeter of the bead in the direction of the ultrasound at the two sides of the bead (which appear at the top and bottom of figure 5(D)): the interior of the arc at the top of the figure appears bright while it is the exterior of the arc at the bottom of the figure that appears bright. The reversal of the shading is a consequence of subtraction—the opposite shading could be produced by reversal of the order of subtraction of the two images.

For our purposes, an analysis of the ultrasound-induced temperature increase in the selected tissue is important. A first approximation of the temperature change is given by

$$\Delta T = \frac{2\mu\nu}{\gamma} I t \tag{9}$$

where μ is the ultrasound attenuation coefficient in soft tissue (= 0.05 cm^{-1} MHz^{-1}), ν is the ultrasound centre frequency (= 1 MHz), γ is the heat capacity per unit volume of soft tissue (= 4 W s cm^{-3} °C^{-1}), I is the ultrasound intensity in W cm^{-2} and t is the application time (15 μs) (Herman and Harris 2002). The maximum intensity can be calculated from the square of our maximum recorded pressure p_{max}^2 using

$$I = \frac{p^2}{2\rho c} \tag{10}$$

where $p_{max}^2 = 1.5 \times 10^{12}$ Pa^2 (Morse 1981). We obtain $I = 5 \times 10^5$ W m^{-2} = 50 W cm^{-2} and a subsequent temperature increase of approximately 1.8×10^{-5} °C. However in our
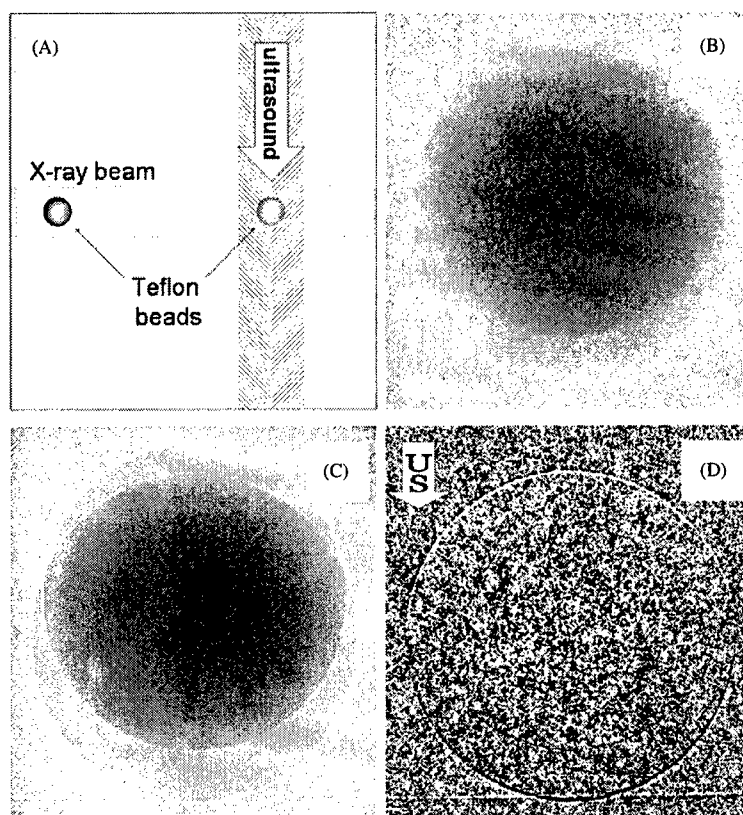
Figure 5. (A) Side view of the sample consisting of two Teflon beads cast in agarose. The two beads are separated by 3 cm. (B) Image of the beads with no phase contrast. (C) Image of the beads with phase contrast. (D) Subtracted image of the two beads. The bead irradiated with ultrasound is nearest the CCD camera and produces a slightly larger image than the bead located outside the sound beam. The x-ray tube voltage for the images was 90 kV. The image in (B) was taken with a 75 s exposure time with the x-ray tube operating at 80 W; the image in (C) was taken with eight times lower tube wattage and eight times longer exposure to give the same total x-ray fluence.

case, *burst* ultrasound, a more specific model which considers an ultrasound–bone interaction should be used as a worst-case scenario. The upper temperature limit for burst ultrasound is approximated by

$$\Delta T = 189.74 \times 10^{-6} I \sqrt{t} \tag{11}$$

with t in s and I in W m^{-2}. Using equation (11) with the same data given above results in an estimated temperature increase of 0.37 °C. It should be noted that since (11) was derived specifically for the case of an ultrasound–bone interface the resulting temperature increase in the case of soft tissue would actually be smaller and would not present any dangers in biological applications.

In order to evaluate the method using tissue-like samples, a phantom of micron-sized agarose objects embedded in chicken breast was examined. The objects in the phantom consisted of pieces of a casting made by mixing carbon nanoparticles with agarose to achieve
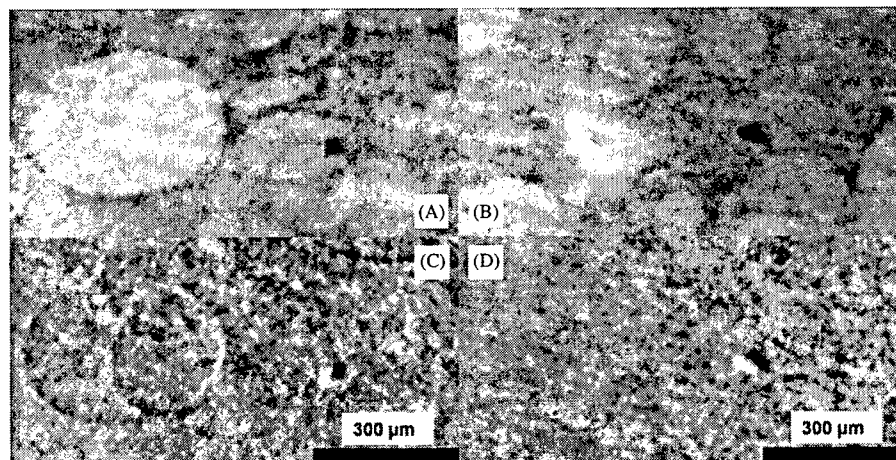
Figure 6. X-ray images of carbon enriched agarose objects embedded in chicken flesh: the round objects are fat bubbles in the chicken flesh. The entire sample is immersed in water. (A) and (B) conventional phase contrast images taken with a 25 μm diameter x-ray source, and (C) and (D) corresponding ultrasound enhanced x-ray phase contrast image.

a density approximately 14% higher than that of the chicken breast, comparable to the density difference between malignant and healthy human breast tissue as reported in Duck (1990), Johns and Yaffe (1987). The conventional phase contrast images in (A) and (B) for two different regions of the phantom show fat globules as being clearly outlined elliptical objects and the agarose objects as the dark masses, their estimated sizes being of the order of 30 $\times$ 30 μm in (A) and 30 $\times$ 60 μm in (B). The ultrasound contrast-enhanced x-ray images corresponding to (A) and (B) are shown in (C) and (D), respectively. Both regions of the phantom were irradiated with ultrasound. The subtracted images are seen to have increased contrast of the agarose objects, and the fat globules as well, highlighting those parts of the phantom displaced by the ultrasound. Both the fat globules and the higher density agarose objects are surrounded with identical shading, indicating motion in the same direction under the influence of the acoustic radiation pressure. Some of the objects, well defined on the images (A) and (B), are no longer visible in subtracted images and can therefore be identified as either artefacts arising from optical imperfections in the sample container or imaging optics. Note that a simple differential shift of two phase contrast images followed by their subtraction, as opposed to the present acoustically modified procedure, would leave artefacts from optical imperfections in the final image.

5. Discussion

The intensity profile of the subtracted image $S(x)$ can be written as $S(x) = I(x + h) - I(x)$ where h is the displacement caused by the application of ultrasound. For small h, it is appropriate to identify the subtracted image as approximately proportional to the space derivative of the phase contrast image in the direction of propagation of the ultrasound, $S(x) = hI'(x)$. As such, low spatial frequency features such as broad absorptions are suppressed in the image while the high frequency features such as those at interfaces between dissimilar materials are emphasized. When the acoustic displacement of an object is of the order of the fringe spacing of the phase contrast, the highlighting of the phase contrast

component of the image is maximal; the image of the object is then almost a pure phase contrast image responsive to changes in density. In general, the contrast in the image is determined by the combined effects of the tissue selectivity of the ultrasound based on differences in acoustic impedance, together with the response of phase contrast to density variation. The resolution, on the other hand, is governed by the parameters of conventional phase contrast imaging, which include the degree of spatial coherence of the x-ray beam and the sample-to-source and sample-to-image distances. A distinctive feature of the method described here is its vector character—the subtracted image shows only those features of the object moved along the propagation direction of the ultrasound, which is evident in figures 5 and 6. Clearly, it is possible to make multiple images where sound is directed from different angles into a body and to process the images to record displacement in more than one direction. Additionally, there are different ultrasound excitation schemes that can be employed leading to, for instance, standing acoustic waves, that can be generated within a body to give contrast dependent on eigenmodes of vibration and other elastic properties of the body, further enhancing the capability of x-rays to probe subtle physical properties of matter.

Acknowledgment

References

Bailat C J, Hamilton T J, Rose-Petruck C and Diebold G J 2004 Acoustic radiation pressure: a 'phase contrast' agent for X-ray phase contrast imaging *Appl. Phys. Let.* submitted
Beckmann F, Bonse U, Busch F and Gunnewig O 1997 X-ray microtomography (microCT) using phase contrast for the investigation of organic matter *J. Comput. Assist. Tomogr.* **21** 539–53
Beyer R T 1978 Radiation pressure—the history of a mislabeled tensor *J. Acoust. Soc. Am.* **63** 1925
Born M and Wolf E 1980 *Principles of Optics* (Oxford: Pergamon)
Chu B and Apfel R E 1982 Acoustic radiation pressure produced by a beam of sound *J. Acoust. Soc. Am.* **72** 1673
Cowley J M 1984 *Diffraction Physics* (Amsterdam: North Holland)
Duck F A 1990 *Physical Properties of Tissue* (London: Academic)
Fatemi M and Greenleaf J F 1998 Ultrasound-stimulated vibro-acoustic spectrography *Science* **280** 82–5
Fulvia Arfelli V B *et al* 2000 Mammography with synchrotron radiation: phase detection techniques *Radiology* **215** 286–93
Gao L, Parker K J, Lerner R M and Levinson S F 1996 Imaging of the elastic properties of tissue—a review *Ultrasound Med. Biol.* **22** 959–77
Herman B A and Harris G R 2002 Models and regulatory considerations for transient temperature rise during diagnostic ultrasound pulses *Ultrasound Med. Biol.* **28** 1217–24
Johns P C and Yaffe M J 1987 X-ray characterisation of normal and neoplastic breast tissues *Phys. Med. Biol.* **32** 675–95
King L V 1934 On the acoustic radiation pressure on spheres *Proc. R. Soc.* A **147** 212–40
Krol A, Ikhlef A, Kieffer J C, Bassano D A, Chamberlain C C, Jiang Z, Pepin H and Prasad S C 1997a Laser-based microfocused x-ray source for mammography: feasibility study *Med. Phys.* **24** 725–32
Krol A, Kieffer J C and Forster E 1997b Laser-driven x-ray source for diagnostic radiology *Proc. SPIE—Int. Soc. Opt. Eng.* **3157** 156–63
McAleavey S A 2003 Estimates of echo correlation and measurement bias in acoustic radiation force impulse imaging *IEEE Trans. Ultrason. Ferroelectr. Freq. Control* **50** 631
Momose A 1995 Demonstration of phase-contrast x-ray computed tomography using an x-ray interferometer *Nucl. Instrum. Methods Phys. Res.* **352** 622–8

4996   T J Hamilton *et al*

Morse P M 1981 *Vibration and Sound* (Acoustical Society of America)

Muthupillai R, Lomas D J, Rossman P J, Greenleaf J F, Manduca A and Ehman R L 1995 Magnetic resonance elastography by direct visualization of propagating acoustic strain waves *Science* **269** 1854–7

Nightingale K, Nightingale R, Palmeri M and Trahey G 1999 *IEEE Ultrason. Symp.* 1319

Nightingale K, Stutz D, Bentley R and Trahey G 2002 *IEEE Symp.* 525

Pogany A, Gao D and Wilkins S W 1997 Contrast and resolution in imaging with microfocus x-ray source *Rev. Sci. Instrum.* **68** 2774

Sarvazyan A P 1998 Shear wave elasticity imaging: a new ultrasonic technology of medical diagnostics *Ultrasound Med. Biol.* **24** 1419

Snigirev A, Snigireva I, Kohn V, Kuznetsov S and Schelokov I 1995 On the possibility of x-ray phase contrast microimaging by coherent high-energy synchrotron radiation *Rev. Sci. Instrum.* **66** 5486

Westervelt P 1951 The theory of steady forces caused by sound waves *J. Acoust. Soc. Am.* **23** 312

Wilkins S W, Gureyev T E, Gao D, Pogany A and Stevenson A W 1996 Phase-contrast imaging using polychromatic hard x-rays *Nature* **384** 335–8